Spectrophotometric properties of galaxies at intermediate redshifts (z~0.2–1.0) I. Sample description, photometric properties and spectral measurements

Fabrice Lamareille, Thierry Contini, Jean-François Le Borgne, Jarle Brinchmann, Stéphane Charlot, Johan Richard

▶ **To cite this version:**

Fabrice Lamareille, Thierry Contini, Jean-François Le Borgne, Jarle Brinchmann, Stéphane Charlot, et al.. Spectrophotometric properties of galaxies at intermediate redshifts (z~0.2–1.0) I. Sample description, photometric properties and spectral measurements. Astronomy and Astrophysics - A&A, 2006, 448, pp.893. 10.1051/0004-6361:20053601 . hal-00013270v3

HAL Id: hal-00013270
https://hal.science/hal-00013270v3

Submitted on 23 Nov 2005

HAL is a multi-disciplinary open access archive for the deposit and dissemination of scientific research documents, whether they are published or not. The documents may come from teaching and research institutions in France or abroad, or from public or private research centers.

L'archive ouverte pluridisciplinaire **HAL**, est destinée au dépôt et à la diffusion de documents scientifiques de niveau recherche, publiés ou non, émanant des établissements d'enseignement et de recherche français ou étrangers, des laboratoires publics ou privés.

Astronomy & Astrophysics manuscript no. aa2005˙3601.hyper31219 23rd November 2005
(DOI: will be inserted by hand later)

ccsd-00013270, version 3 - 23 Nov 2005

Spectrophotometric properties of galaxies at intermediate redshifts (z˜0.2–1.0)⋆

I. Sample description, photometric properties and spectral measurements⋆⋆

F. Lamareille[1], T. Contini[1], J.-F. Le Borgne[1], J. Brinchmann[2,3], S. Charlot[2,4], and J. Richard[1]

[1] Laboratoire d'Astrophysique de Toulouse et Tarbes (LATT - UMR 5572), Observatoire Midi-Pyrénées, 14 avenue E. Belin, F-31400 Toulouse, France
[2] Max-Planck Institut für Astrophysik, Karl-Schwarzschild-Strasse 1 Postfach 1317, D-85741 Garching, Germany
[3] Centro de Astrofísica da Universidade do Porto, Rua das Estrelas - 4150-762 Porto, Portugal
[4] Institut d'Astrophysique de Paris, CNRS, 98 bis Boulevard Arago, F-75014 Paris, France

Received ; Accepted

Abstract We present the spectrophotometric properties of a sample of 141 emission-line galaxies at redshifts in the range $0.2 < z < 1.0$ with a peak around $z \in [0.2, 0.4]$. The analysis is based on medium resolution ($R_s = 500 - 600$), optical spectra obtained at VLT and Keck. The targets are mostly "Canada-France Redshift Survey" emission-line galaxies, with the addition of field galaxies randomly selected behind lensing clusters. We complement this sample with galaxy spectra from the "Gemini Deep Deep Survey" public data release. We have computed absolute magnitudes of the galaxies and measured the line fluxes and equivalent widths of the main emission/absorption lines. The last two have been measured after careful subtraction of the fitted stellar continuum using the `platefit` software originally developed for the SDSS and adapted to our data. We present a careful comparison of this software with the results of manual measurements. The pipeline has also been tested on lower resolution spectra, typical of the "VIMOS/VLT Deep Survey" ($R_s = 250$), by resampling our medium resolution spectra. We show that we can successfully deblend the most important strong emission lines. These data are primarily used to perform a spectral classification of the galaxies in order to distinguish star-forming galaxies from AGNs. Among the initial sample of 141 emission-line galaxies, we find 7 Seyfert 2 (narrow-line AGN), 115 star-forming galaxies and 16 "candidate" star-forming galaxies. Scientific analysis of these data, in terms of chemical abundances, stellar populations, etc, will be presented in subsequent papers of this serie.

Key words. galaxies: abundances – galaxies: evolution – galaxies: fundamental parameters – galaxies: starburst.

1. Introduction

Understanding the major steps in the evolution of galaxies still remains a great challenge to modern astrophysics. While the general theoretical framework of the hierarchical growth of structures in the universe including the build up of galaxies is well in place, this picture remains largely unconstrained by observations, especially at high redshifts. Statistically significant samples of galaxies, from the local Universe to the highest redshifts, are crucial to constrain the models of galaxy formation and evolution. Indeed, comparing the physical properties (star formation rate, extinction, chemical abundances, kinematics, mass, stellar populations, etc) of galaxies at different epochs will allow us to study the evolution with redshift of fundamental scaling relations such as the Luminosity-Metallicity or the Tully-Fisher relations and hence put strong constraints on galaxy formation and evolution models.

Thanks to recent massive surveys ("Sloan Digital Sky Survey" SDSS, Abazajian et al. 2003, 2004; "2degree Field Galaxy Redshift Survey" 2dFGRS, Colless et al. 2001), large spectroscopic samples of galaxies are now available in the local universe, giving access to the detailed physical properties of galaxies as a function of their environment for more than ∼ 100 000 of them. Similar massive spectroscopic surveys are being carried out on the largest ground-based telescopes to explore the high-redshift ($0.2 < z < 4$) universe (e.g. "VIMOS/VLT Deep Survey" VVDS, Le Fevre et al. 2003; "Deep Extragalactic Evolutionary Probe" DEEP, Koo & DEEP Team 2002; etc...). The main goal of these surveys is to study

Send offprint requests to: F. Lamareille, e-mail: `flamare@ast.obs-mip.fr`

⋆ Based on observations collected at the Very Large Telescope, European Southern Observatory, Paranal, Chile (ESO Programs 64.O-0439, 65.O-0367, 67.B-0255, 69.A-0358, and 72.A-0603)

⋆⋆ Tables 6,7,8 and 9 are only available in electronic form at the CDS via anonymous ftp to cdsarc.u-strasbg.fr (130.79.128.5) or via http://cdsweb.u-strasbg.fr/cgi-bin/qcat?J/A+A/

the evolution of galaxies, large-scale structures, and Active Galactic Nuclei (AGN) over more than 90% of the current age of the universe (e.g. Le Fèvre et al. 2004). Most previous studies of intermediate-redshift ($z \sim 0.2 - 1$) galaxies have been driven by the "Canada-France Redshift Survey" (CFRS, Lilly et al. 1995) which produced a unique sample of 591 field galaxies with $I_{AB} < 22.5$ in the range $0 < z < 1.4$ with a median redshift of ~ 0.56 (Lilly et al. 1995). Deep multicolor (B, V, I and K) photometry is available for most galaxies and several objects have been observed with the Hubble Space Telescope (HST, Brinchmann et al. 1998) providing useful complementary informations on the morphology (Lilly et al. 1998; Schade et al. 1999) and the level of interactions (Le Fèvre et al. 2000) of galaxies up to $z \sim 1$. This survey has been, for some years, a unique tool for statistical studies of the evolution of field galaxies as a function of redshift. However, because of the low spectral resolution ($\Delta\lambda \sim 40$Å) and limited signal-to-noise ratio (hereafter SNR) of original CFRS spectra, no reliable estimate of crucial physical properties, such as chemical abundances and reddening, have been determined from these data.

Subsequent spectrophotometric studies of intermediate-redshift galaxies have been performed by various authors on smaller samples (e.g. Guzman et al. 1997; Kobulnicky & Zaritsky 1999; Hammer et al. 2001; Contini et al. 2002; Lilly et al. 2003; Kobulnicky et al. 2003; Liang et al. 2004a,b; Maier et al. 2004). Most of these studies were focused on galaxies with either a peculiar morphology (e.g. compact and luminous galaxies; Guzman et al. 1997; Hammer et al. 2001) or selected in a special wavelength domain: UV-bright (Contini et al. 2002), infrared-bright (Liang et al. 2004a), or narrow-band selected galaxies (Maier et al. 2004).

Thanks to the new class of multi-object spectrograph and to the associated large and deep surveys (VVDS, DEEP, etc), a large amount of spectrophotometric data will now become available. One of the goals of this paper is to review all the technical issues that can be involved in the reduction and analysis process of these large datasets, together with the scientific results that can be drawn from these studies. This will allow us to define a standard pipeline with particular care taken to optimise it for the VVDS.

This paper builds up on previous work dedicated to the spectrophotometric analysis of SDSS data (e.g. Tremonti et al. 2004; Brinchmann et al. 2004), in which a large part of the pipeline has been described already. In this paper, we describe how we adapt the existing pipeline to the study of intermediate-redshift galaxies observed at a lower spectral resolution and SNR than the SDSS galaxies. In order to do that, we defined a sample of $\sim$ 140 galaxies at intermediate redshifts ($0.2 < z < 1.0$) showing a large range of physical properties. Using medium-resolution optical spectra mainly acquired with the FORS (FOcal Reducer Spectrograph) instruments on the VLT, we derived their spectrophotometric properties, with a particular attention on defining an automatic process which will be mandatory to analyze large surveys. We also investigate the effect of spectral resolution on the derived quantities, as large surveys like VVDS are based on low-resolution spectra.

This first paper focuses on the general reduction pipeline, photometric properties and emission-line measurements. The scientific analysis of this sample in terms of stellar populations, chemical abundances, etc, will be presented in subsequent papers.

This paper is organized as follow: we first describe our sample in Sect. 2, and then the observations and associated data reduction in Sect. 3. We present the spectroscopic analysis in Sect. 4 and the photometric data in Sect. 5. Finally we perform a spectral classification of our sources in Sect. 6.

2. Sample description

2.1. The parent samples

The CFRS produced a large and homogeneous sample of field galaxies with measured redshifts and morphological properties. This gives us the opportunity to select interesting galaxies at intermediate redshifts in order to acquire new spectra with a better spectral resolution and SNR than the original ones. We thus decided to select and re-observe a sub-sample of CFRS galaxies selected in three of the five CFRS fields visible from Paranal (Chile), namely CFRS 0000+00 (hereafter CFRS00), CFRS 0300+00 (hereafter CFRS03), and CFRS 2215+00 (hereafter CFRS22). In addition to this main sample, we acquired spectra for some new and unidentified galaxies selected to fill the slits in the FORS masks. This sample of 63 galaxies is called the "CFRS sub-sample" (see Table 1).

In addition, we decided to take advantage of some series of spectra previously observed by the "Galaxies" team in Toulouse and their collaborators. They were essentially samples of galaxies inside massive lensing clusters, but, in order to complete the masks, some foreground or background field galaxies were observed. These 48 field galaxies form the "CLUST sub-sample" (see Table 2).

Finally, we added a sample of public available spectra from the "Gemini Deep Deep Survey" (GDDS, Abraham et al. 2004) to cover the high redshift end (i.e. $0.4 < z < 1.0$). We selected 31 emission-line spectra which form the "GDDS sub-sample" (see Table 3).

2.2. Selection criteria

The main goal of our program is to probe the physical properties of star-forming galaxies at intermediate redshifts. We thus selected, among the CFRS sub-sample, galaxies with narrow emission lines as quoted in the literature, thus excluding galaxies with broad Balmer emission lines typical of AGN. In order to obtain spectra with a sufficient SNR in a reasonable exposure time, we limited ourselves to galaxies brighter than an apparent V-band magnitude $V_{AB} = 23$ (on the CFRS sub-sample). In order to fill the MOS masks, some galaxies without emission lines were also observed. Although we will not include these objects in the present analysis, their spectra have been reduced for possible future use. After the basic data reduction process (see Sect. 3), we selected only the spectra with "visible" (i.e. from visual examination, signal-to-noise ratio of at least 5) emission lines and a good overall SNR of the continuum (at least 10). We also want the spectrum to show at

Table 1. The CFRS sub-sample. *(a)* Unique identification number (this work, please use the acronym "LCL05", for reference). *(b)* CFRS id if available. *(c)* Redshift (see Sect. 3.2 for redshift determination). *(d)* Signal-to-noise ratio of the continuum at $\sim$ 5500Å or $\sim$ 3500Å (noted by the symbol *). *(e)* Maximum signal-to-noise ratio of the strongest emission line. *(f)* 'a' flag means the emission lines were manually measured on this spectrum, 'c' flag means this spectrum was a combination of two observations.

LCL05[a]	CFRS[b]	J2000 (α, δ)	z[c]	S/N$_c$[d]	S/N$_m$[e]	f
field: CFRS00						
001		00 02 46.93 − 00 39 01	0.3405	7.2	17	a
002		00 02 43.10 − 00 40 48	0.6157	7.3*	23	a
003		00 02 41.53 − 00 40 01	0.3409	11.1	58	a
004	00.0852	00 02 39.83 − 00 41 02	0.2682	13.1	50	a
005	00.0861	00 02 39.41 − 00 41 40	0.2682	19.7	19	
006	00.0900	00 02 37.06 − 00 40 36	0.2470	8.7	33	a
007	00.0940	00 02 35.58 − 00 41 06	0.2694	13.5	26	
008	00.1013	00 02 32.97 − 00 41 33	0.2437	7.5	34	
009	00.0124	00 02 29.91 − 00 41 42	0.2880	8.5	16	
010	00.0148	00 02 28.19 − 00 41 16	0.2672	14.0	39	c
011	00.1726	00 02 48.51 − 00 41 35	0.2959	16.1	55	a
012	00.0699	00 02 44.91 − 00 41 23	0.0874	11.6	17	
013		00 02 44.59 − 00 39 52	0.2489	11.2	21	a
014		00 02 38.75 − 00 40 21	0.3902	7.2	7	a
015	00.1057	00 02 34.15 − 00 41 31	0.2432	5.8	30	a
016	00.0121	00 02 30.16 − 00 41 35	0.2975	12.8	228	a
017	00.0229	00 02 23.26 − 00 41 23	0.2453	13.9	18	
field: CFRS03						
018	03.1184	03 02 49.28 + 00 13 37	0.2046	7.3	30	c
019	03.1343	03 02 49.56 + 00 11 58	0.1889	5.0	33	
020	03.0442	03 02 44.89 + 00 13 45	0.4781	6.3*	27	c
021	03.0476	03 02 43.11 + 00 14 13	0.2601	13.4	73	ac
022	03.0488	03 02 42.16 + 00 13 24	0.6049	5.6*	38	a
023	03.0507	03 02 40.44 + 00 14 03	0.4648	6.9*	30	
024	03.0523	03 02 39.34 + 00 13 27	0.6532	7.0*	47	ac
025	03.0578	03 02 35.19 + 00 14 10	0.2188	7.4	32	
026	03.0605	03 02 33.01 + 00 14 07	0.2189	9.6	54	ac
027	03.0003	03 02 31.85 + 00 13 18	0.2186	4.3	46	ac
028	03.0037	03 02 29.48 + 00 14 13	0.1744	26.0	86	ac
029	03.0046	03 02 28.67 + 00 13 33	0.5123	5.5*	18	c
030	03.0085	03 02 25.24 + 00 13 24	0.6083	4.1*	23	c
031	03.0096	03 02 24.29 + 00 12 28	0.2189	7.8	60	ac
field: CFRS22						
032	22.0502	22 17 58.26 + 00 14 29	0.4682	6.0	15	
033	22.0585	22 17 55.60 + 00 16 59	0.2940	11.9	32	c
034	22.0671	22 17 53.03 + 00 18 27	0.3175	15.5	67	ac
035	22.0819	22 17 48.76 + 00 17 18	0.2910	10.4	36	ac
036	22.0855	22 17 47.88 + 00 16 28	0.2105	13.6	100	a
037	22.0975	22 17 45.12 + 00 14 47	0.4189	6.8	21	
038	22.1013	22 17 44.31 + 00 15 05	0.2307	14.4	76	a
039	22.1084	22 17 42.53 + 00 14 21	0.2928	16.3	52	ac
040	22.1203	22 17 39.54 + 00 15 25	0.5384	9.5*	69	c
052	22.0474	22 17 58.70 + 00 21 11	0.2794	8.0	119	a
053	22.0504	22 17 58.07 + 00 21 37	0.5382	10.9*	66	a
054	22.0637	22 17 54.01 + 00 21 26	0.5422	16.4*	83	a
055	22.0642	22 17 53.77 + 00 22 05	0.4687	3.7*	10	a
056	22.0717	22 17 51.63 + 00 21 46	0.2787	19.6	38	
057	22.0823	22 17 48.57 + 00 21 27	0.3333	24.6	28	
058	22.1082	22 17 42.49 + 00 21 05	0.2918	4.7	71	
059		22 17 44.00 + 00 23 21	0.2765	8.6	28	a
060	22.1144	22 17 40.75 + 00 21 46	0.3586	5.0	21	a
061	22.1220	22 17 38.82 + 00 21 19	0.3583	8.9	29	a
062	22.1231	22 17 38.42 + 00 22 13	0.2846	16.8	82	a
063	22.1309	22 17 36.18 + 00 21 24	0.2847	5.2	23	
041		22 17 53.01 + 00 19 14	0.2164	2.7	9	
042		22 17 53.48 + 00 19 25	0.3524	2.2	22	a
043	22.0622	22 17 54.58 + 00 16 58	0.3237	6.4	20	
044		22 17 46.54 + 00 17 13	0.2764	19.9	24	
045	22.0919	22 17 46.48 + 00 16 53	0.4712	6.1*	158	ac
046		22 17 46.99 + 00 16 23	0.6515	7.3*	35	
047		22 17 47.12 + 00 16 26	0.4716	2.8*	24	
048	22.0903	22 17 46.76 + 00 15 45	0.2948	4.6	22	c
049	22.0832	22 17 48.44 + 00 15 15	0.2306	25.1	91	ac
050	22.1064	22 17 43.08 + 00 15 08	0.5369	4.4*	42	ac
051	22.1339	22 17 35.39 + 00 14 34	0.3842	6.1*	78	ac

Table 2. The CLUST sub-sample. Same legend as Table 1. *(g)* alternative identification number if available (LBP2003: Le Borgne et al. 2003, CBB2001: Couch et al. 2001, CPK2001: Campusano et al. 2001, SKK2001: Smail et al. 2001).

LCL05[a]	alt[g]	J2000 (α, δ)	z[c]	S/N$_c$[d]	S/N$_m$[e]
field: a2218					
136	SKK2001 368	16 35 59.12 + 66 12 01.3	0.6926	4.0*	17
137	SKK2001 159	16 35 45.02 + 66 12 44.7	0.4730	5.7*	24
138		16 35 40.48 + 66 13 06.0	0.4491	1.4	6
field: a2390					
064		21 53 38.10 + 17 43 48.0	0.2412	13.6	70
065		21 53 40.01 + 17 44 07.2	0.0665	6.1	214
066		21 53 28.00 + 17 39 01.1	0.4261	1.0	8
067		21 53 25.34 + 17 39 44.4	0.4500	3.3	10
068		21 53 30.42 + 17 39 16.4	0.6291	2.6*	11
069		21 53 26.84 + 17 40 43.4	0.2213	6.8	38
070		21 53 29.30 + 17 40 26.8	0.7392	6.1*	27
071		21 53 33.45 + 17 40 53.2	0.5263	3.9	29
072		21 53 39.42 + 17 43 50.6	0.3425	4.8	15
141		21 53 33.02 + 17 41 56.8	0.3982	5.7	33
field: a963					
139		10 17 04.82 + 39 02 27.2	0.7307	1.2	27
140		10 17 04.57 + 39 02 25.3	0.7307	2.4	25
field: ac114					
073	LBP2003 b	22 58 37.19 − 34 49 27.8	0.2605	10.6	42
074		22 58 43.42 − 34 48 04.8	0.0965	13.7	253
075	CBB2001 796	22 58 54.75 − 34 48 26.8	0.0985	10.2	28
076	LBP2003 h	22 58 43.35 − 34 49 36.5	0.3207	21.5	54
077	LBP2003 c	22 58 43.07 − 34 48 48.1	0.2999	19.8	47
078	CPK2001 V7	22 58 45.60 − 34 49 03.9	0.5669	9.3*	27
079	CPK2001 V6	22 58 50.94 − 34 47 26.5	0.4095	5.0*	16
080	CBB2001 688	22 58 41.83 − 34 49 06.1	0.3304	8.5	34
081	CPK2001 V11	22 58 57.46 − 34 47 06.8	0.3805	2.5	13
082	CPK2001 V9	22 58 56.56 − 34 46 58.6	0.4121	7.2*	17
083		22 58 54.94 − 34 46 32.6	0.7262	11.7*	111
084	CBB2001 453	22 58 37.48 − 34 50 16.2	0.4100	4.2*	24
085		22 58 35.92 − 34 49 26.9	0.7186	3.0*	20
086		22 58 35.20 − 34 48 59.0	0.4125	2.6	11
087		22 58 42.52 − 34 49 26.8	0.4092	1.3*	9
088		22 58 41.11 − 34 48 48.2	0.7571	4.8*	70
field: cl1358					
142		13 59 48.33 + 62 31 18.4	0.4069	1.6	72
field: cl2244					
089		22 47 14.75 − 02 03 25.1	0.5628	5.8*	23
090		22 47 14.63 − 02 08 12.9	0.5651	5.4*	34
091		22 47 13.62 − 02 07 36.5	0.7865	7.8*	27
092		22 47 08.58 − 02 07 05.4	0.3289	4.6	57
093		22 47 08.35 − 02 06 38.8	0.6402	5.1*	36
094		22 47 07.04 − 02 04 28.6	0.5701	2.4*	17
095		22 47 09.56 − 02 07 15.7	0.3416	3.9	13
096		22 47 14.16 − 02 06 51.8	0.4386	3.3*	15
097		22 47 11.35 − 02 06 29.6	0.5724	4.8*	17
098		22 47 11.08 − 02 06 19.5	0.5717	2.9*	15
field: j1206					
099		12 06 13.71 − 08 51 01.3	0.3555	7.9	21
100		12 06 10.29 − 08 45 53.7	0.3547	5.6	26
101		12 06 09.66 − 08 50 44.4	0.3547	8.6	18
102		12 06 10.97 − 08 50 22.3	0.4280	10.0	13
103		12 06 13.18 − 08 48 26.8	0.4759	6.6	21
104		12 06 07.74 − 08 47 21.2	0.4522	5.2*	19

least [OII]λ3727, Hβ and [OIII]λ5007 lines in order to derive the metallicity of the galaxies.

We do not aim to construct any volume-limited, magnitude-limited, or emission-line flux-limited sample. Our main concern is to build a sample of star-forming galaxies selected by their bright emission lines. However, we must point out that this selection criterion introduces some biases. First the very high or very low metallicity objects will not be selected (i.e. [OIII] lines are too weak). Second, very dusty and thus very strongly reddened galaxies are not selected in our sample.

Table 3. The GDDS sub-sample. Same legend as Table 1.

LCL05[a]	GDDS id	J2000 (α, δ)	z
field: NOAO-Cetus			
105	02-0452	02 09 49.51 – 04 40 24.49	0.828
106	02-0585	02 09 50.13 – 04 40 07.55	0.825
107	02-0756	02 09 43.49 – 04 39 43.11	0.864
108	02-0995	02 09 48.09 – 04 38 54.39	0.786
109	02-1134	02 09 44.46 – 04 38 33.46	0.913
110	02-1724	02 09 37.13 – 04 36 02.61	0.996
field: NTT Deep			
111	12-5337	12 05 18.75 – 07 24 57.19	0.679
112	12-5513	12 05 16.62 – 07 24 43.70	0.611
113	12-5685	12 05 15.21 – 07 24 28.16	0.960
114	12-5722	12 05 20.96 – 07 24 22.27	0.841
115	12-6456	12 05 19.15 – 07 23 45.64	0.612
116	12-6800	12 05 18.14 – 07 23 21.97	0.615
117	12-7099	12 05 26.34 – 07 22 53.02	0.567
118	12-7205	12 05 15.47 – 07 22 58.00	0.568
119	12-7660	12 05 26.83 – 07 22 07.83	0.791
120	12-7939	12 05 31.39 – 07 20 37.77	0.664
121	12-8250	12 05 17.24 – 07 20 02.97	0.767
field: SA22			
122	22-0040	22 17 32.22 + 00 12 45.91	0.818
123	22-0145	22 17 47.08 + 00 13 17.40	0.754
124	22-0563	22 17 36.84 + 00 15 27.22	0.787
125	22-0619	22 17 45.85 + 00 16 42.48	0.673
126	22-0630	22 17 32.36 + 00 16 16.28	0.753
127	22-0643	22 17 38.32 + 00 16 59.41	0.788
128	22-0751	22 17 46.55 + 00 16 26.68	0.471
129	22-0926	22 17 31.36 + 00 17 48.10	0.786
130	22-1534	22 17 37.87 + 00 17 45.88	0.470
131	22-1674	22 17 49.22 + 00 17 14.32	0.879
132	22-2196	22 17 44.16 + 00 15 21.56	0.627
133	22-2491	22 17 37.66 + 00 14 12.38	0.471
134	22-2541	22 17 32.94 + 00 13 58.92	0.617
135	22-2639	22 17 46.70 + 00 13 31.93	0.883

3. Spectroscopic data

3.1. Observations and data reduction

Spectrophotometric observations of the "CFRS sub-sample" were performed during two observing runs (periods P65 and P67) with the ESO/VLT at Paranal (Chile). Two nights (July 1st and August 28th, 2000) were devoted to the first run (ESO 65.O-0367) during which we observed three masks: two in the CFRS22 field and one in the CFRS00 field. We used the FORS1 spectrograph mounted on the ANTU unit of the VLT. The exposure time for each mask was divided into four exposures of 40mn, leading to a total exposure time per mask of 2h40mn. Two other nights (June 25th and September 13th, 2001) were allocated for the second run (ESO 67.B-0255). For this run, we used both the FORS1 and FORS2 spectrograph mounted on the ANTU and KUEYEN units of the VLT respectively. We observed three more masks: one in the CFRS22 field (total exposure time = 8 × 25mn = 3h20mn), one in the CFRS00 field (total exposure time = 6 × 25mn = 2h30mn), and one in the CFRS03 field (total exposure time = 8 × 25mn = 3h20mn).

The instrumental configuration was the same for all the observations. MOS masks have been produced using the FIMS software. Pre-images (5mn exposure time in $r_{\rm Gunn}$ band) for each field have been acquired for an accurate positioning and orientation of the MOS masks. The GRIS300V grism has been used to cover a total possible wavelength range of ∼ 4500–8500 Å with a resolution $R_{\rm s}$ = 500. The effective wavelength range depends on the position of the slit/galaxy in the MOS mask, being shorter at the edges of the mask. The slit width was 1″ yielding a nominal resolution of ∼ 15 Å. The GG435+31 light blocking filter was used to avoid any second-order contamination in the red part of the spectrum.

Most spectra of the "CLUST sub-sample" have been obtained during the run ESO 072.A-0603 with FORS2 on VLT/KUEYEN dedicated to the observation of background galaxies magnified by massive clusters. As the main targets do not fill the whole masks, slits have been designed on cluster and foreground galaxies, as well as background unmagnified galaxies. The clusters observed were Abell 2390, AC 114 and Clg 2244-02 (hereafter Cl2244). FORS2 in MXU mode has been used with the GRIS300V grism and an order sorting filter GG375, allowing a useful wavelength range from 4000 Å to 8600 Å, and yielding a wavelength resolution of $R_{\rm s}$ = 500. The observations were made in service mode between August 29th and September 3rd, 2003. For each cluster mask, a total exposure time of ∼ 4h was obtained. A 1″ slit width was used for each slit. Similar spectra were obtained on April 11th 2002 during a visitor mode run (ESO 69.A-0358) on cluster MACS J1206.2-0847 (hereafter J1206) with the FORS1 spectrograph on VLT/MELIPAL (see Ebeling et al., in preparation). The GRIS300V grism and a 1"-width slit were used, yielding a wavelength coverage between ∼ 4000 Å and 8600 Å, and a wavelength resolution of $R_{\rm s}$ = 500. An order sorting filter GG375 was used. The total exposure time was 38mn. The additional AC 114 data were obtained on October 5, 1999 during the run ESO 64.O-0439 with FORS1 on VLT/ANTU (UT1) telescope. The same G300V and 1"-width slit were used. These observations were also part of a program to study magnified background galaxies. The wavelength coverage is ˜4000–8000 Å and the resulting resolution 500. Depending on the mask used, the exposure times were 2h15mn, 1h30mn or 1h17mn (see Campusano et al. 2001).

The remaining spectra in the "CLUST sub-sample" (with LCL05# ≥ 136) are more magnified objects serendipitously found during a long-slit search for Lyman-α emitters at high redshift along the critical lines of the clusters Abell 963, Abell 2218, Abell 2390 and Clg 1358+62 (Santos et al. 2004; Ellis et al. 2001). The double-beam Low Resolution Imaging Spectrograph (LRIS, Oke et al. 1995) was used on the Keck telescope with a 1"-width long and 175"-length long slit, a 600-line grating blazed at λ 7500 Å (resolution ∼ 3.0 Å) for the red channel and a 300-line grism blazed at 5000 Å with a dichroic at 6800 Å (resolution ∼ 3.5–4.0 Å) for the blue channel of the instrument. More details on these observations are given in Santos et al. (2004).

Data reduction was performed in a standard way with IRAF packages. In particular, the extraction of the 1D spectra and the computation of SNR for each spectrum have been performed with the IRAF package `apall`. The wavelength calibration used He-Ar arc lamps and flux calibration have been done using spectrophotometric standard stars observed each night. Two examples of FORS spectra of CFRS galaxies are shown in Fig. 1.

Spectroscopic observations of the GDDS sub-sample have been done with GMOS spectrograph on the Gemini North telescope between August 2002 and August 2003. The spectra cover a typical wavelength range of 5500 Å to 9200 Å

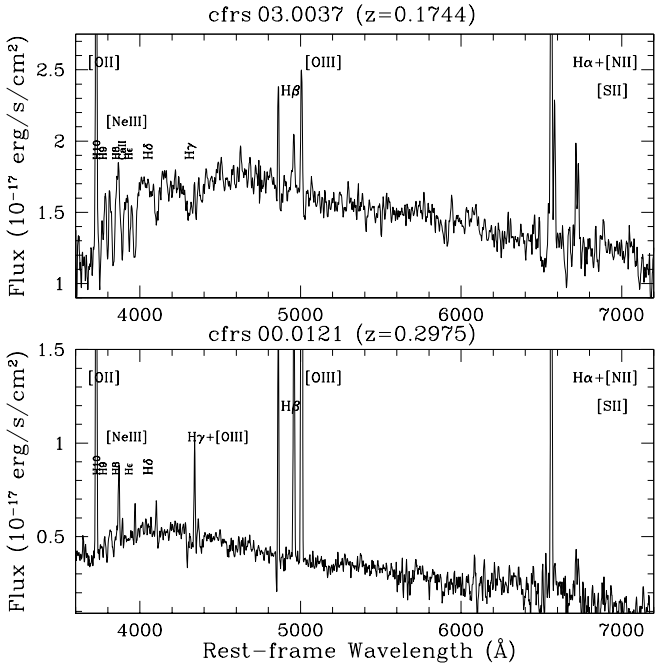

Figure 1. Examples of VLT/FORS spectra of intermediate-redshift CFRS galaxies. Bottom panel: a low-metallicity galaxy (CFRS 00.0121) with a high collisional excitation degree. Top panel: a high-metallicity galaxy (CFRS 03.0037). The position of the brightest emission lines is indicated.

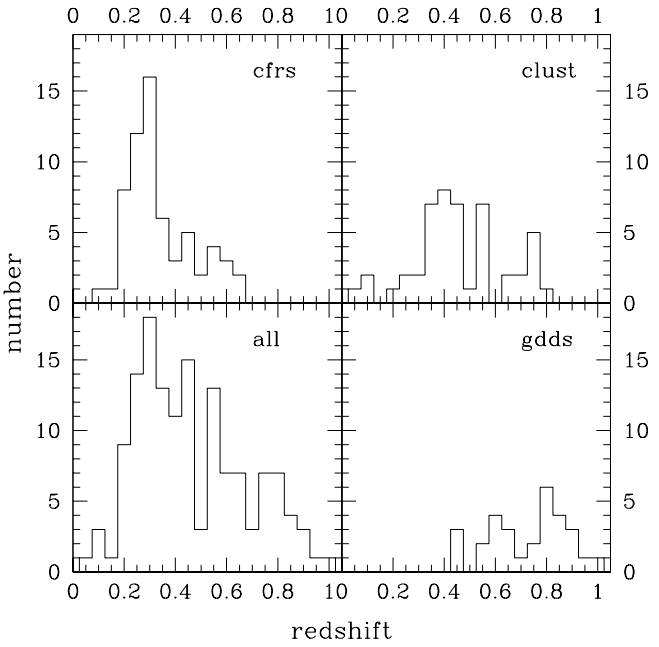

Figure 2. Redshift histogram of our sample of intermediate-redshift galaxies (bottom-left: all sample, top-left: "CFRS sub-samble", top-right: "CLUST sub-sample", bottom-right: "GDDS sub-sample"). The number of galaxies is calculated per 0.05 redshift bin.

with a wavelength resolution of approximately $R_s \approx 630$ (see Abraham et al. 2004 for full details).

The spectroscopic observation details are summarized in Table 4.

3.2. Redshift distribution

The redshift of galaxies were derived using the centroid of the brightest emission lines: [OII]λ3727, [OIII]λ5007, Hβ and Hα when available. In case of doubt, we tried to adjust a stellar template to the continuum. Our redshifts agree with the published ones to within 1% for the re-observed CFRS galaxies.

Fig. 2 shows the histogram of the measured redshifts. The redshift distribution is dominated by galaxies in the range $z \in [0.2, 0.4]$. This is a result of our selection criteria which favor galaxies showing both [OII]λ3727 and Hα emission lines. This population is complemented by a number of galaxies with $z \in [0.4, 1.0]$ leaving us with a statistically significant, although not complete, sample of 141 galaxies spanning the redshift range 0.2 to 1.0.

4. Spectroscopic analysis

4.1. Continuum fitting and subtraction

4.1.1. The software

For the spectral fitting we have adapted the `platefit` IDL code developed primarily by C. Tremonti. The code is discussed in detail in Tremonti et al. (2004), but for the benefit of the reader we outline the key features here.

The continuum fitting is done by fitting a combination of model template spectra (discussed below) to the observed spectrum with a non-negative linear least squares fitting routine. The strong emission lines are all masked out when carrying out this fit. The fitted continuum is then subtracted from the object spectrum together with smoothed continuum correction to take out minor spectrophotometric uncertainties. The residual spectrum contains the emission lines.

The fit to the emission lines is carried out by fitting Gaussians in velocity space to an adjustable list of lines. All forbidden lines are tied to have the same velocity dispersion and all Balmer lines are also tied together to have the same velocity dispersion. This improves the fit for low SNR lines, but for the present sample this is not of major importance. The weak [NII]λ6548 and [NII]λ6584 emission lines, which are closed to the Hα emission line at our working resolution, are tied together so that the line ratio [NII]λ6584/[NII]λ6548 is equal to the theoretical value 3. The [OII]$\lambda\lambda$3726,3729 line doublet is measured as one [OII]λ3727 emission line, with a velocity dispersion freely fitted between 1.0 and 2.0 times the velocity dispersion of the other forbidden lines, which reproduces the broadening effect of two narrow lines blended together. `platefit` returns the equivalent widths, fluxes and associated errors for all fitted lines as well as other information.

The pipeline was optimised for SDSS spectra so some precautions must be taken when using it on other data sets. In particular it is important to have a reliable error estimate for each

Table 4. Summary of spectroscopic observations.

LCL05 ids	instrument/telescope	run	λ range (Å)	resolution	slit width/lentgh	exposure time
001-010	FORS1 / VLT	65.O-0367	4500-8500	R_s = 500	1" / 22"	4x40mn
010-017	FORS2 / VLT	67.B-0255	4500-8500	R_s = 500	1" / 22"	6x25mn
018-031	FORS1 / VLT	67.B-0255	4500-8500	R_s = 500	1" / 22"	2x25mn
018-031(c)	FORS2 / VLT	67.B-0255	4500-8500	R_s = 500	1" / 22"	6x25mn
032-040	FORS1 / VLT	65.O-0367	4500-8500	R_s = 500	1" / 22"	4x40mn
033-040(c) / 042-051	FORS2 / VLT	67.B-0255	4500-8500	R_s = 500	1" / 22"	6x25mn
034-040(c) / 041 / 045-051(c)	FORS1 / VLT	67.B-0255	4500-8500	R_s = 500	1" / 22"	2x25mn
052-063	FORS1 / VLT	65.O-0367	4500-8500	R_s = 500	1" / 22"	4x40mn
064-072 / 083-098	FORS2 / VLT	72.A-0603	4000-8600	R_s = 500	1" / 22"	∼4h
073-082	FORS1 / VLT	64.O-0439	4000-8000	R_s = 500	1" / 22"	2h15mn, 1h30mn or 1h17mn
099-104	FORS1 / VLT	69.A-0358	4000-8600	R_s = 500	1" / 22"	38mn
136 / 142	LRIS / Keck	2001A	3800-10 000	$R_s \approx 2000$	1" / 175"	33mn
137-140	LRIS / Keck	2002A	3800-10 000	$R_s \approx 2000$	1" / 175"	33mn
141	LRIS / Keck	2002B	3800-10 000	$R_s \approx 2000$	1" / 175"	33mn
105-135	GMOS / Gemini	GDDS	5500-9200	$R_s \approx 630$		

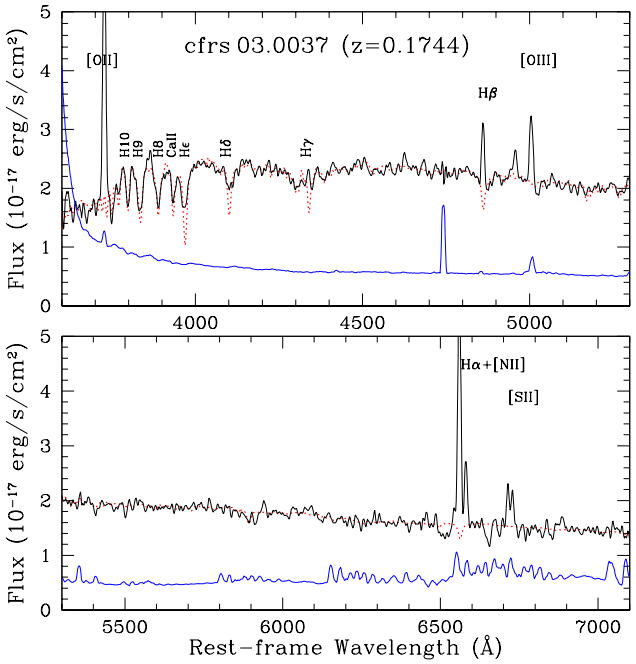

Figure 3. Example of input spectrum for the CFRS 03.0037 galaxy at $z = 0.1744$. The solid line shows the observed spectrum, the blue line the error spectrum (magnified 5 times) and the red dotted line shows the continuum fitting.

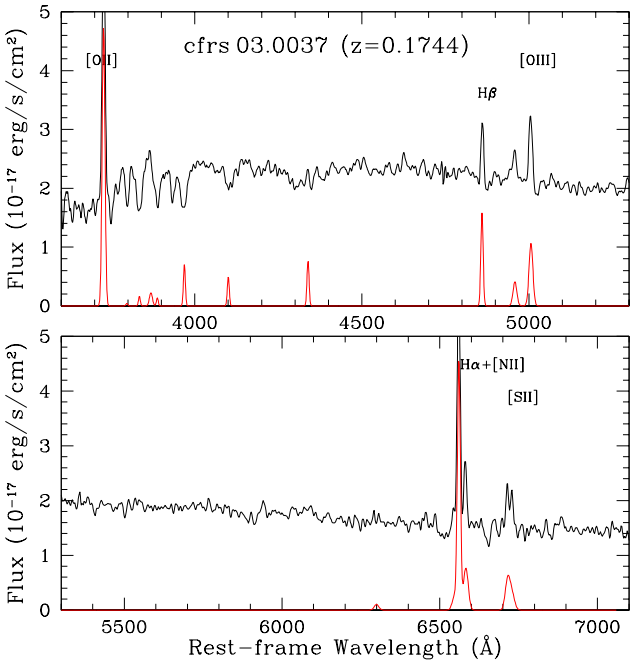

Figure 4. Example of emission-line fits, done after the continuum subtraction for the CFRS 03.0037 galaxy at $z = 0.1744$.

pixel (i.e. the error spectrum, see Fig. 3) and to mask out regions of the spectra which are unreliable. Failure to do so will severely affect the continuum fitting.

The software returns a set of new spectra (sampled in velocity space): the continuum spectrum which is the fitted linear combination of the model templates added to the smoothed continuum (see Fig. 3), the flux-continuum spectrum which is the raw spectrum with the stellar continuum subtracted, the nebular spectrum which is built by adding all the emission-line fits together (see Fig. 4), and finally the stellar spectrum which is the raw spectrum with the nebular one subtracted (note that this only take into account the lines which are included in the fitting).

4.1.2. Model templates

The template spectra used to fit the continuum emission of the galaxy in `platefit` were produced using the Bruzual & Charlot (2003) population synthesis model[1]. At wavelengths between 3200 and 9500 Å, the template spectra rely on the STELIB stellar spectral library (Le Borgne et al. 2003), for which the resolution is about 3 Å FWHM.

The template spectra were chosen in order to represent, through non-negative linear combinations, the properties of galaxies with any star formation history and metallicity. Specifically, the spectra were selected to provide good coverage of SDSS-DR1 galaxies in the plane defined by the 4000 Å break and the Hδ stellar absorption line strength, which are good indicators of the star formation history of a galaxy

[1] These template spectra are included in the original model release package.

(e.g., Kauffmann et al. 2003b). The library includes 10 template spectra for each of the three metallicities $Z = 0.2\,Z_\odot$, $Z_\odot$ and $2.5\,Z_\odot$. The spectra correspond to 10 instantaneous-burst models with ages of 0.005, 0.025, 0.10, 0.29, 0.64, 0.90, 1.4, 2.5, 5, and 11 Gyr.

4.2. Adaptation to non-SDSS spectra and measurement of emission lines

We have created an interface procedure which facilitates the analysis of our non-SDSS spectra with the `platefit` routines. The input spectra are provided as two FITS files each: one for the spectrum itself and another one for the error spectrum, the output spectra are written into ASCII files and the measurements are provided in a FITS table. The behaviour of the interface procedure is controlled by a parameter file which is an extension of that used in the `platefit` code and which controls the operation of the code.

The result of flux and equivalent-width measurements of the main emission lines is shown in Table 8 and in Table 9.

4.2.1. Comparison with manual determination

It is instructive to compare the performance of the automatic fitting code with manual measurements of line fluxes using standard methods. To this end we measured emission lines from a subsample of the spectra using the task `splot` in IRAF. This subsample is made of the 31 first reduced spectra, that do not show any specific properties, among the CFRS sub-sample (see Table 1). In this section we will compare these manual results to the automatically computed ones. We expect to see significant differences for the Balmer lines where it is difficult to adjust for the contribution of the underlying stellar absorption when doing manual fitting. In contrast the measurements for the forbidden lines should be consistent within the errors as the effects of absorption lines for these is much less.

In Figure 5, we compare the automatic (using `platefit`) and manual measurements (using IRAF task `splot`) of oxygen emission-line equivalent widths (top panels) and fluxes (bottom panels). Figure 5 shows that there is a very good agreement between manual and automatic measurements for two of the strongest emission lines: [OII]λ3727 and [OIII]λ5007. Almost every point fall on the $y = x$ line and we also remark that the error estimates are consistent between the two methods. By comparing the bottom to the top panels, we see that the agreement is good both for equivalent-width or for line-flux measurements.

In Figure 6, we now compare the automatic and manual measurements of equivalent widths for Balmer emission lines (top panels) and low-intensity forbidden emission lines ([NII]λ6584 and [SII]λ6717, bottom panels). Figure 6 shows clearly the need to use `platefit` in order to have a good estimate of the Balmer emission lines. As we see in the top-left panel, manual measurements significantly underestimate the flux in the Hβ emission line where underlying stellar absorption is normally not negligible in our galaxies. We note however that the difference between manual and automatic measurements for the Hα emission line is smaller, which is to be expected since the underlying absorption is similar to that at Hβ, but the emission flux is considerably higher. The bottom panels show the same comparison for the fainter [NII]λ6584 and [SII]λ6717 emission lines. The dispersion here is larger but the measurements are consistent within the errors.

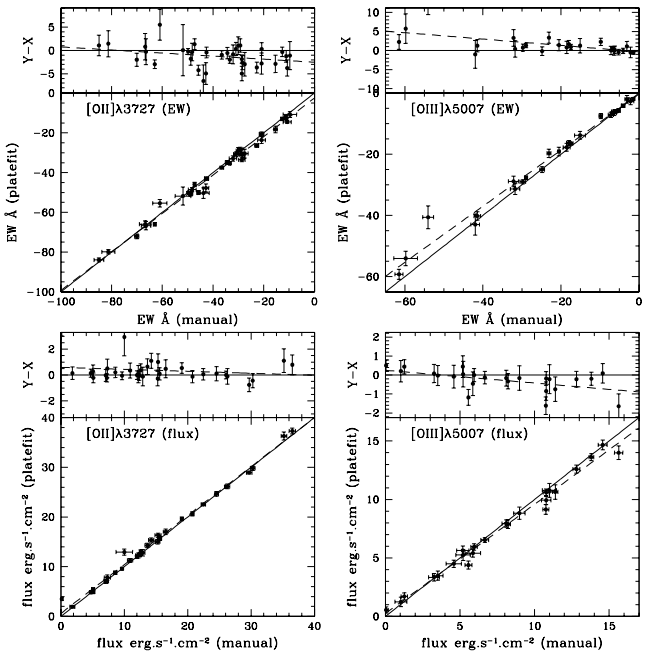

Figure 5. Comparison between oxygen emission lines measured automatically (using `platefit`) and manually (using IRAF task `splot`). Top panels: [OII]λ3727 (left) and [OIII]λ5007 (right) equivalent widths (in Å) given by `platefit` as a function of the manual measurement. Bottom panels: same for the measurements of line fluxes (in 10^{-17} erg s^{-1} cm^{-2}). The solid line is the $x = y$ line and the dashed line is the linear regression.

Two features are based on two blended emission lines each at our working resolution: the doublet [SII]$\lambda\lambda$6717+6731 and the line ratio [NII]λ6584/Hα. In Figure 7, we compare the automatic and manual measurements of these blended features (EWs: top panels, fluxes: bottom panels). Figure 7 illustrates the performance of `platefit` in deblending these lines. We see that `platefit` is able to give good results for the measurement of these low-intensity blended emission lines. To reach this level of accuracy we had to modify the way the equivalent width was estimated by `platefit`, which was optimised for higher resolution spectra. We tested various methods, and found that the best results were obtained when we calculated the equivalent width taking the continuum from the smoothed continuum spectra and combined this with the emission line flux. This allows us to make use of the line information in other parts of the spectrum to overcome the blending problems and we get a very good agreement between the measurements at different spectral resolutions as we will see below.

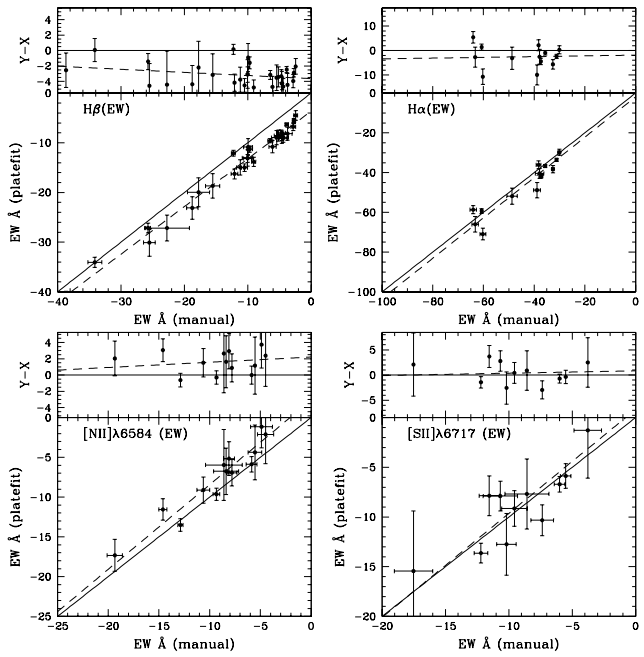

Figure 6. Comparison between equivalent widths (in Å) for the Balmer (top panels) and [Nii]λ6584, [Sii]λ6717 (bottom panels) emission lines measured automatically (using `platefit`) and manually (using IRAF task `splot`). The solid line is the $x = y$ line and the dashed line is the linear regression.

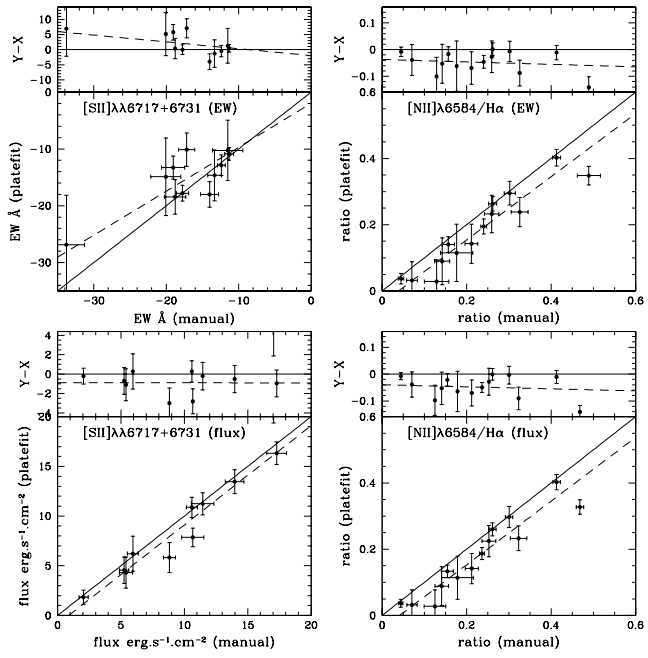

Figure 7. Comparison between blended features computed from equivalent width (in Å, top panels) and from fluxes (in 10^{-17} erg s^{-1} cm^{-2}, bottom panels) automatically (using `platefit`) and manually (using IRAF task `splot`): the line sum [Sii]$\lambda\lambda$6717+6731 (left) and the line ratio [Nii]λ6584/Hα (right). The solid line is the $x = y$ line and the dashed line is the linear regression.

Table 5. Calculations of the mean and the rms of the difference between downgraded resolution and original resolution measurements. We give first the absolute values, and then the relative values which are more physically significant in percent (*rel.* columns). We compare these results to the mean of the error on the original data (two last columns).

parameter	mean	*rel.*	rms	*rel.*	err	*rel.*
EW([Oii]λ3727)	−0.30Å	3.3%	2.09Å	9.8%	1.21Å	8.2%
EW(Hα)	+0.51Å	0.5%	3.32Å	9.0%	1.95Å	9.2%
EW([Nii]λ6584)	+0.69Å	12%	1.92Å	24%	1.93Å	47%
[Nii]λ6584/Hα	−0.02	11%	0.05	23%	0.05	47%
log([Nii]λ6584/Hα)	−0.06 dex	8.2%	0.12 dex	16%	0.20 dex	21%

4.2.2. Resolution accuracy

To prepare for the spectral analysis of upcoming deep surveys, such as VVDS, we have used our medium resolution data to test the behaviour of `platefit` when used on spectra with a lower resolution. This point will be critical in particular for the [Nii]λ6584/Hα ratio, as these two lines are blended in low-resolution spectra ($R_s \lesssim 313$). The main issue is to determine if we can use this ratio to perform any spectral classification (see Sect. 6) and metallicity estimate (van Zee et al. 1998; Pettini & Pagel 2004). Our sample is approximatively at the spectral resolution $R_s = 500$, while the resolution of the VVDS is $R_s = 250$. Thus, we have downgraded the resolution of our spectra by a factor of two with a gaussian convolution, and we have rerun `platefit` on the new spectra.

Table 5 shows the difference between downgraded resolution and original resolution measurements for some characteristic lines. We see that the rms of the relative difference is low and strictly less than the error associated on each line. We also remark that there are some systematic shifts (i.e. the mean value of the difference is not null) but they are still lower than the error. Figure 8 shows that there is no dependence with the line intensity. For low resolution spectra, we reach a higher level of accuracy by tiding up the velocity dispersion of all the emission lines together, whatever they are forbidden or Balmer lines. This implies the assumption that all broad-line AGNs have been taken out of the sample before running the `platefit` software (see Sect. 6 below for a detailed discussion about the various spectral types of emission-line galaxies).

The [Nii]λ6584/Hα line ratio as measured on the downgraded spectra is compared to the original measurements in Fig. 9 (see also Table 5). It is clear that the difference is small and consistent with zero within the errors. The logarithm of this line ratio, which is used for metallicity estimates, also has a weak dependence on the spectral resolution, and the scatter is lower than the standard error on metallicity calibrations (~ 0.2 dex).

5. Photometric analysis

5.1. Photometric data

We measured the photometric magnitudes with SExtractor (Bertin & Arnouts 1996) in the *R* band using the pre-imaging data. We used an input file with all the image coordinates of the galaxies and we computed the photometric magnitudes us-

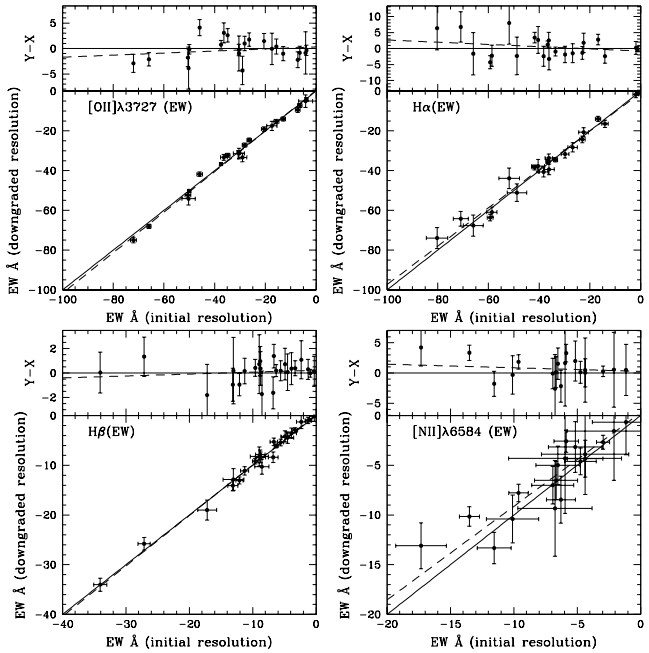

Figure 8. Comparison between the equivalent width (in Å) of [Oii]λ3727 (top-left), Hα (top-right), Hβ (bottom-left) and [Nii]λ6584 (bottom-right) measured at downgraded (R_s = 250) and original (R_s = 500) resolutions. The solid line is the $x = y$ line and the dashed line is the linear regression.

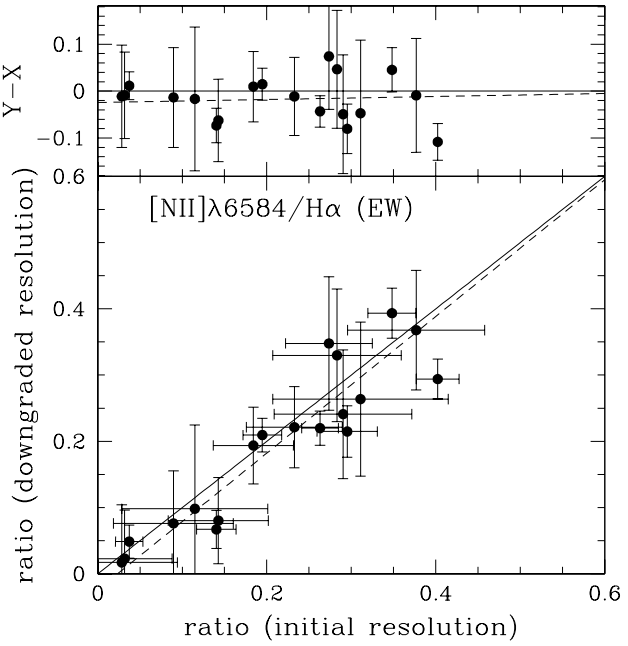

Figure 9. Comparison between the [Nii]λ6584/Hα line ratio calculated with the equivalent widths measured at downgraded (R_s = 250) and original (R_s = 500) resolutions. The solid line is the $x = y$ line and the dashed line is the linear regression.

ing the best radial adjustment (`MAG_BEST` parameter). We adopt these measurements in place of those from the literature for the CFRS sub-sample to ensure consistency with the CLUST sub-sample.

For the CFRS sub-sample, the pre-imaging was performed in the Gunn *R* band with the VLT/FORS1 camera. For the CLUST sub-sample, pre-images have been acquired in the Bessel *R* band with the FORS1 camera, except for the J1206 field, for which the pre-imaging has been done with the TEK2048 camera on the UH88in telescope in the *R* band. For the LRIS data, we used observations of Abell 963, Abell 2218, Abell 2390 with the CFH12k camera at CFHT (Czoske et al. 2002) in the *I* band. For the cluster Clg 1358+62, we measured photometry on an HST-WFPC image in the *F*606*W* band.

The photometric calibration was performed in different ways depending on the field. The J1206 field was already calibrated. The other fields from the CLUST sub-sample were calibrated using a photometric standard star. For the CFRS sub-sample, the standard star was observed in a different filter than the galaxies (Bessel *R* rather than Gunn *R*), preventing us from using it to do the calibration. Fortunately we were able to take advantage of the previously measured magnitudes of the CFRS galaxies in the *I* band (CFHT FOCAM camera): the Bessel *R* magnitudes of these objects were computed using spectroscopic colors (see Sect. 5.2), and we calculated the zero-point of each image by doing a linear regression.

The photometric magnitudes of the GDDS sub-sample were directly taken from the literature (Chen et al. 2002): *R* band photometry of the NTT Deep field has been taken with the BTC camera on the Cerro Tololo Inter-American Observatory (CTIO) 4m telescope, *I* band photometry of the NOAO-Cetus and SA22 fields have been taken with the CFH12k camera on the Canada France Hawaii Telescope (CFHT).

5.2. Spectroscopic magnitudes

We want to compute spectroscopic magnitudes, by integrating the flux through a set of filter response curves, in order to have information on the color (we only have photometric magnitudes in the *R* band), on the *k*-correction and on the aperture differences (i.e. the amount of flux lost because of the limited size of the slits during spectroscopic observations) of our galaxies.

We used an adaptation of the `filter_thru` routine from the SDSS IDL library[2]. For a flux-calibrated spectrum this routine returns a spectroscopic magnitude in the *AB* system (Oke 1974). If the spectrum does not cover the full bandwidth of the filter (borders at 5%), it returns nothing. We computed spectroscopic magnitudes directly from the observed spectrum if it covers the full bandwidth of the filter, otherwise from the model spectrum given by the continuum fitting.

We used the filter response curve of the FORS1 camera (CCD + atmosphere) for the following bands: Bessel *B*, *V*, *R* and *I*. We also have the filter response of the FORS1 camera in the Gunn *R* band (used for the pre-imaging of the CFRS fields), of the TEK2048 camera in the *R* band (used for the pre-imaging of the J1206 field), of the CFHT FOCAM camera in the *I* band

[2] `http://spectro.princeton.edu`

(used for the original CFRS data), and of the BTC camera in the *R* band and the CFH12k camera in the *I* band (used for the photometry of the GDDS sub-sample). Finally we also calculated the photometry in the *u*, *g*, *r*, and *i* color system of the SDSS for possible comparison (Fukugita et al. 1996). We have checked that the spectroscopic colors are in good agreement (i.e. within the error bars) with published photometric colors.

We can use the information of the continuum SNR from Tables 1 and 2 to have an estimate of the uncertainties of the spectroscopic magnitudes. We use the following formula:

$$\Delta m \approx \frac{2.5}{\ln 10}\mathrm{SNR}^{-1}$$

We find a mean uncertainty of ~ 0.1 magnitudes.

5.3. Absolute magnitudes

The absolute magnitudes were computed using photometric magnitudes and the *k*-correction given from spectroscopic magnitudes (see Sect. 5.2). If we want, for example, the absolute magnitude in the *I* band ($M_{\mathrm{AB}}(I)$) given a photometric magnitude in the *R* band (R_{AB}), we use the following formula:

$$M_{\mathrm{AB}}(I) = d + R_{\mathrm{AB}} + \left(I^{\mathrm{rest}}_{\mathrm{spec}} - R^{\mathrm{obs}}_{\mathrm{spec}}\right)$$

where d is the distance modulus, $I^{\mathrm{rest}}_{\mathrm{spec}}$ and $R^{\mathrm{obs}}_{\mathrm{spec}}$ are the spectroscopic magnitudes computed respectively in rest-frame and in observed-frame so that $I^{\mathrm{rest}}_{\mathrm{spec}} - R^{\mathrm{obs}}_{\mathrm{spec}}$ is the *k*-correction. Note that we can alternatively write:

$$M_{\mathrm{AB}}(I) = d + I^{\mathrm{rest}}_{\mathrm{spec}} + \left(R_{\mathrm{AB}} - R^{\mathrm{obs}}_{\mathrm{spec}}\right)$$

where $R_{\mathrm{AB}} - R^{\mathrm{obs}}_{\mathrm{spec}}$ is the aperture difference. We remark that the aperture difference (*ape* in Table 6) is less than -1.3 mag for a large majority of our sample, which means that the aperture coverage is at least 30% of the galaxy total luminosity. This avoids important disk/bulge effects (see Kewley et al. 2005 for details). The distance modulus is calculated using the last cosmology given by WMAP (Spergel et al. 2003): $H_0 = 71$ km s^{-1} Mpc^{-1}, $\Omega_\Lambda = 0.73$ and $\Omega_{\mathrm{m}} = 0.27$. The following formula gives the distance modulus as a function of the redshift z:

$$d = -5\log\left(\frac{c}{H_0 \cdot 10\mathrm{pc}} \cdot (1+z) \cdot \int_0^z f(z')^{-1/2} dz'\right)$$

where $f(z') = (1+z')^2(1+\Omega_{\mathrm{m}}z') - \Omega_\Lambda z'(2+z')$.

The photometric magnitudes (R_{AB} and I^0_{AB} in Table 6) are not corrected for foreground extinction whereas this is necessary for future scientific analysis. We thus take into account the foreground dust extinction from the Milky Way by using the Schlegel et al. (1998) dust maps (A_I in Table 6) for computing the rest-frame colors and the absolute magnitude.

5.4. Lensing corrections

For the galaxies in the CLUST sub-sample, we need to correct for the magnification effect caused by the gravitational lensing of the cluster. We do this using the most recent mass models for the galaxy clusters in this sample (for AC 114: Natarajan et al. 1998; Campusano et al. 2001; for Abell 2390: Pelló et al. 1999; for Cl 2244: Kneib et al., unpublished; for Abell 2218: Kneib et al. 1996; Ellis et al. 2001; for Abell 963: Smith et al. 2003; for Clg 1358:Franx et al. 1997). We derived the magnification at the redshift of our background sources with the LENSTOOL software developed by Kneib (1993). The corrections due to the lensing are usually small (< 0.3 mags) compared with the photometric errors. For sources very close to the mean redshift of the cluster (for example in J 1206) no correction was applied.

The results are provided in Table 6. The *I*-band absolute magnitude is given after correction for the foreground dust extinction, the *k*-correction and the lensing effect. We calculate the absolute magnitude in any others bands using the given spectroscopic colors.

5.5. Color-color diagrams

To gain some insight into the nature of the galaxy population in our sample, we start by constructing the $g-r$ versus $u-g$ color-color diagram (see Fig. 10). Strateva et al. (2001) has shown that this diagram separates galaxies into early and late types. We expect to see irregulars with a blue continuum at low $u-g$ and $g-r$ colors, whereas ellipticals, which have a substantial Balmer break, should have "red" $u-g$ and $g-r$ colours. To ease interpretation we use rest-frame colours throughout.

Figure 10 shows that our galaxy sub-samples are well distributed within the late-type region showing mainly irregular or Sc "color" types. The proportion of early-type spirals is much less and we have only a few ellipticals. This figure thus indicates that the latest spectral types are more likely to be observed, as confirmed by the histogram shown in Fig. 11. This result is primarily due to our selection criterion as we biased our sample in favor of emission-line galaxies. Indeed irregular galaxies usually have brighter emission lines than Sb galaxies, so they will be in our sample down to very low SNR. In contrast galaxies of (spectral) type Sb will only be included in our sample when their spectrum is of good SNR. Any possible effect introduced by this bias will have to be taken into account in subsequent analysis.

We must however remark that neither Fig. 10 nor Fig. 11 are accurate enough to determine which galaxy is of a given spectral type because of the high dispersion of the $u-r$ values for each spectral type (e.g. the effect of internal dust on the colors).

6. Spectral classification

6.1. Nature of the main ionizing source

As we want to focus the scientific analysis on star-forming galaxies, we have to make the difference between starbursts and AGNs which both show emission lines in their spectrum. The AGN population can be divided into three main types: Seyfert 1, Seyfert 2 and LINERs. The Seyfert 1, also called broad-line AGNs, can be excluded from our sample by comparing the FWHM of the Balmer emission lines to the FWHM of the forbidden lines: those galaxies with a significantly higher FWHM for the Balmer lines are expected to be Seyfert 1. The ratio of

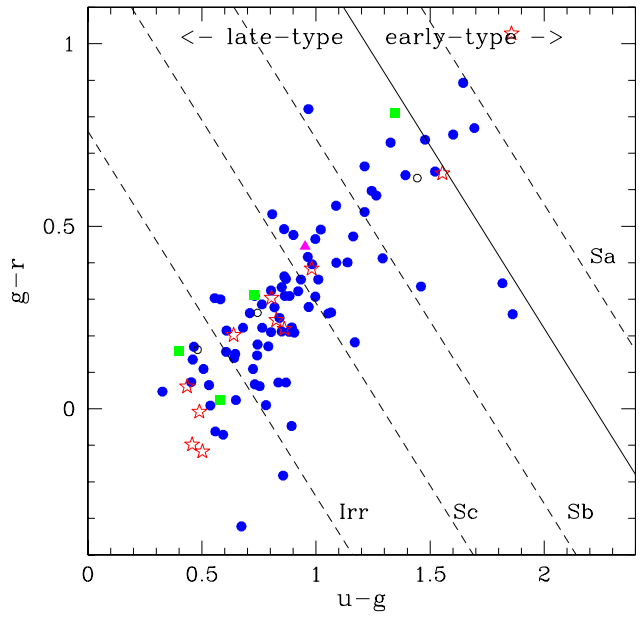

Figure 10. Rest-frame color-color diagram using SDSS passbands. The solid line shows the empirical separation ($u-r=2.22$) between late-type (below the line) and early-type (above the line) galaxies from Strateva et al. (2001). The dotted lines shows the mean value of the $u-r$ parameter for standard spectra of the Sa, Sb, Sc and Irr spectral types: respectively 2.56, 1.74, 1.29 and 0.76 (Strateva et al. 2001). The different symbols indicate star-forming galaxies and AGNs as determined in Sect. 6 (see the description of the symbols in Fig. 14).

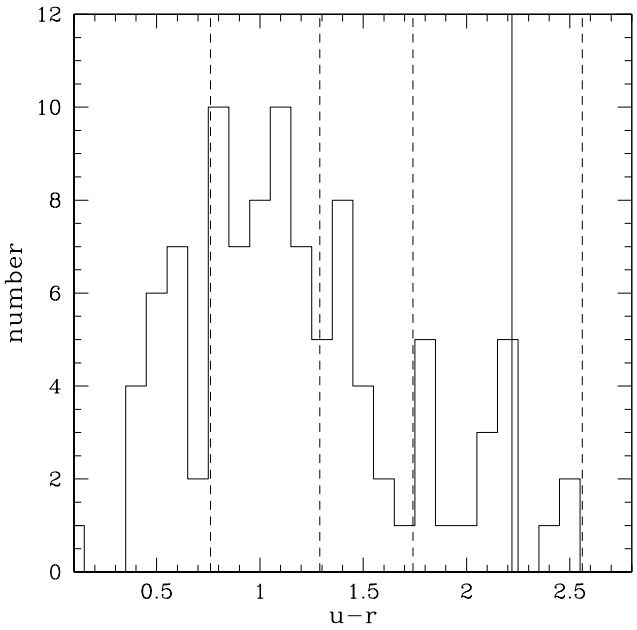

Figure 11. Histogram of the rest-frame $u-r$ color. We plot the number of galaxies per 0.1 bin of the $u-r$ as an indicator of the spectral type. The solid and dotted lines are the same as in Fig. 10.

the FWHM of the Balmer lines to that of the forbidden lines is consistent with unity for most of our sample galaxies (mean of 0.98 with a rms scatter of 0.18). We found 6 peculiar objects showing Balmer lines significantly broader than forbidden ones ($FWHM_{\rm Balmer}/FWHM_{\rm forbidden}\sim 2-3$). These objects could be classified as Seyfert 1 galaxies. However, after a careful visual inspection of individual spectra, we found that the measurement of the FWHM of the Balmer lines in these galaxies is disrupted by either weak Balmer emission lines or noise features. These objects are thus classified as narrow emission-line galaxies.

6.2. Diagnostic diagrams

6.2.1. "Red" diagnostics diagrams

We still need to separate star-forming galaxies from narrow-line AGNs, namely Seyfert 2 and LINERs. Seyfert 2 have a high excitation degree compared to LINERs. The standard prescription (Veilleux & Osterbrock 1987) makes use of the [NII]λ6584/Hα, [SII]$\lambda\lambda$6717+6731/Hα and [OIII]λ5007/Hβ line ratios to separate the star-forming galaxies from AGNs; and the [OIII]λ5007/Hβ as an indicator of the ionization level to distinguish Seyfert 2 from LINERs.

The standard diagnostic diagrams are shown in Fig. 12 for the [NII] diagnostic and in Fig. 13 for the [SII] diagnostic. The limit between star-forming galaxies and AGNs are given by Kewley et al. (2001) (+ 0.15dex for the [SII] diagnostic in order to take into account the model uncertainties). The star-forming galaxies are well separated from AGNs and follow a clear sequence covering a large range of ionization levels and collisional excitation degrees. The classification is obvious, i.e. the [NII] and [SII] diagnostics are in agreement, for 37 galaxies: 34 are star-forming galaxies and 3 are Seyfert 2.

6.2.2. "Blue" diagnostic diagrams

As recently pointed by Lamareille et al. (2004), we can also use the "blue" emission lines (i.e. [OII]λ3727, [OIII]λ5007 and Hβ) to perform the spectral classification for higher redshift galaxies (i.e. with no observable Hα and [NII]λ6584 "red" lines) but with a lower accuracy. We note that 104 galaxies (73.8% of our sample) can only be classified with the blue diagnostics. The blue diagnostic diagrams are shown in Fig. 14 and in Fig. 15. Please note that we use theses diagrams without any correction for dust extinction (as calibrated on 2dFGRS data), by the use of equivalent widths instead of fluxes (see Sect. 6.2.3 below).

We found four objects (LCL05 045, LCL05 065, LCL05 109, and LCL05 142), very close in the R_{23} vs. O_{32} classification (four points on top of Fig. 15), which are classified as Seyfert 2 according to this diagram. However this classification is not in agreement with i) the "red" classification as star-forming galaxy that we derive for one of them (LCL05 065), ii) with the overall aspect of their spectra

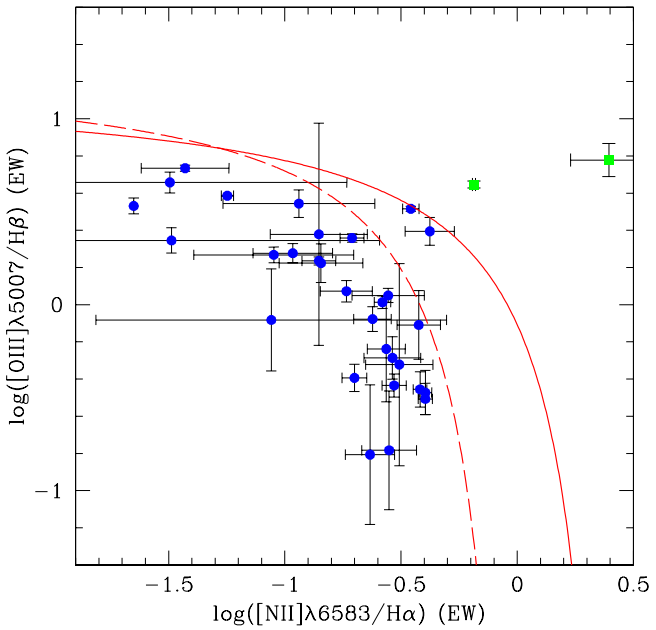

Figure 12. Standard diagnostic diagram using the [NII]λ6584/Hα emission-line ratio. Blue circles identify star-forming galaxies, green squares indicate AGNs (Seyfert 2) and magenta triangles show contradictory cases (see text for details). The solid line shows the theoretical limit from Kewley et al. (2001). The dashed line is the empirical limit from Kauffmann et al. (2003a) for SDSS galaxies.

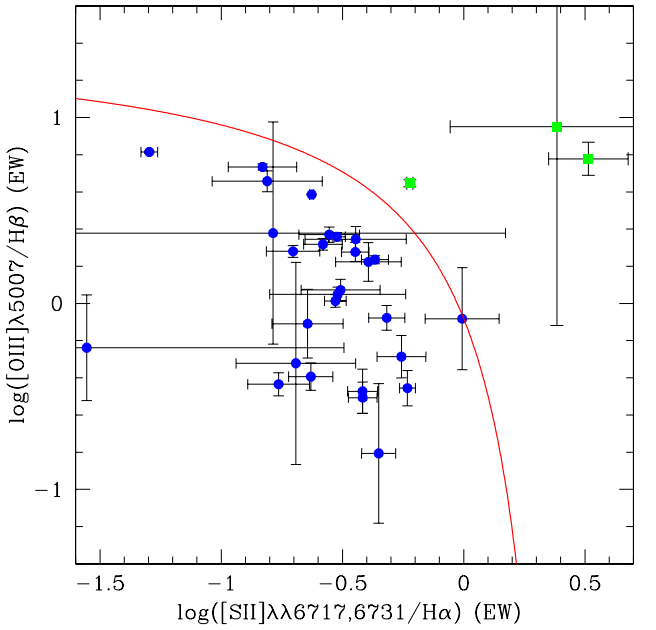

Figure 13. Standard diagnostic diagram using the [SII]$\lambda\lambda$6717+6731/Hα emission-line ratio. Same legend as in Fig. 12.

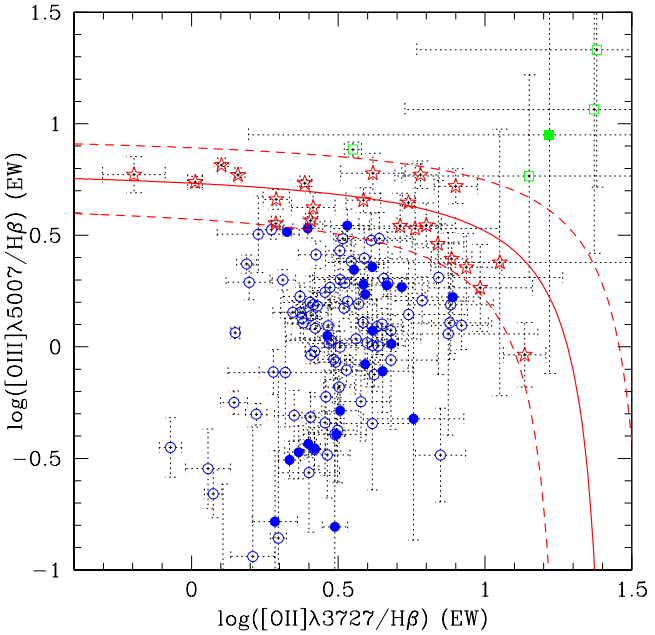

Figure 14. "Blue" diagnostic diagram. The symbols show the results of the "blue" diagnostic: blue circles for star-forming galaxies, green squares for AGNs (Seyfert 2), magenta triangles for contradictory cases and red stars for unclassified objects. Filled symbols are for objects already classified with standard diagnostic diagrams. The solid line shows the empirical calibration from Lamareille et al. (2004) and the dashed lines the associated error domain.

(very faint continuum and high ionization state typical of HII galaxies), or with the low [NII]/Hα ratio estimated recently from NIR spectroscopy for LCL05 045 (Maier et al. 2005). We conclude that the R_{23} vs. O_{32} "blue" classification, calibrated on the 2dFGRS data, may not be valid on its upper part. For these four objects, we keep only the results from the [OIII]λ5007/Hβ vs. [OII]λ3727/Hβ classification, i.e. *candidate* star-forming galaxies (see below).

We found four objects (LCL05 017, LCL05 097, LCL05 115, and LCL05 130) which are classified as Seyfert 2 galaxies but with very high error bars on the diagnostic diagrams. These objects show noisy spectra and/or undetected Hβ emission line (while oxygen lines are detected). Therefore their classification as Seyfert 2 is not fully secure.

We have a number of objects which fall into the error domain on the two "blue" diagrams and are thus unclassified. After checking their spectra, we decided to keep them in our sample as *candidate* star-forming galaxies, keeping in mind in the subsequent analysis that their emission-line spectrum could be contaminated by a low-luminosity AGN.

We finally find 115 (81.6%) "secure" star-forming galaxies, 7 (5.0%) Seyfert 2, 16 (11.3%) "candidate" star-forming galaxies, and 3 (2.1%) objects which are still unclassified (i.e. they have one or more missing lines). Results are shown in Table 7.

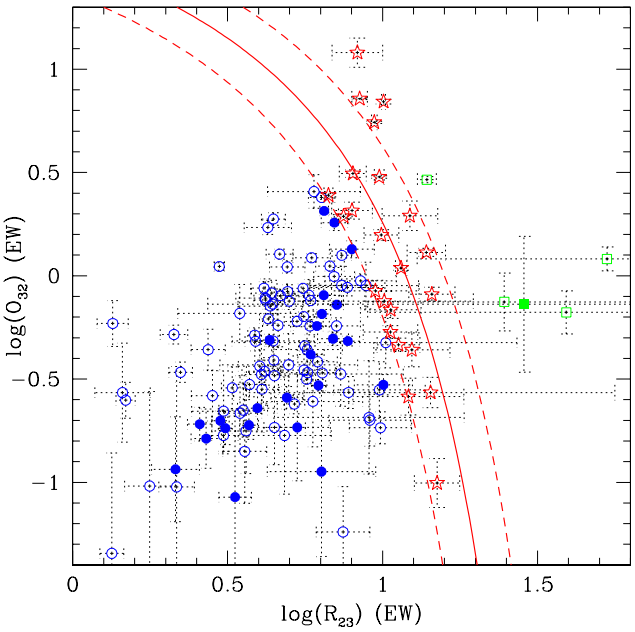

Figure 15. Another "blue" diagnostic diagram. Same legend as in Fig. 14.

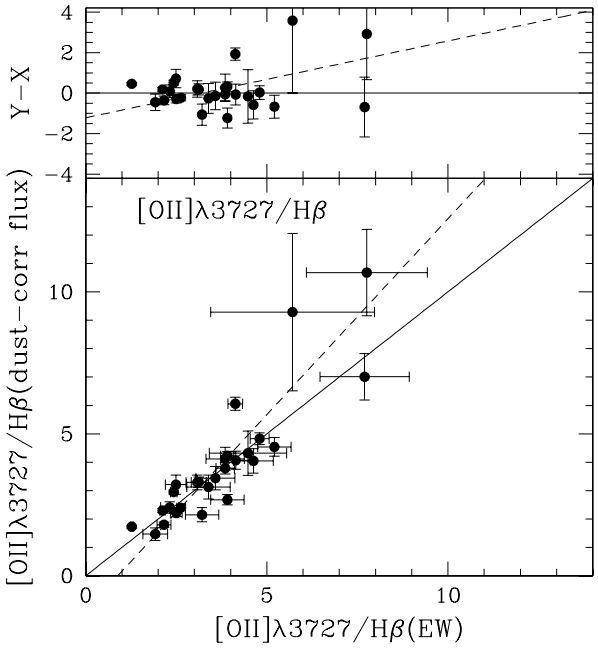

Figure 16. Comparison between the equivalent-width (*x*-axis) and dust-corrected flux (*y*-axis) ratio of [OII]λ3727 and Hβ emission lines. The solid line shows the $y = x$ curve and the dashed line is the fit to the data.

6.2.3. Discussion on dust extinction

The "red" diagnostic diagram makes use of various line ratios which are all insensitive to the dust extinction because they involve emission lines with similar wavelengths ([NII]λ6548, [SII]$\lambda\lambda$6717,6731 and Hα in one case, [OIII]$\lambda\lambda$4959,5007 and Hβ in the other case). This is not the case for the "blue" diagnostic diagrams which make use of the [OII]λ3727 and Hβ emission lines in the same ratio. These diagrams can then be strongly affected by the dust extinction.

The effect of dust is minimized by the use of equivalent width measurements instead of fluxes. Indeed no correction for reddening is needed on equivalent width ratios, if we assume that the attenuation in the continuum and emission lines is the same. To check this assumption, we have derived dust extinction values from the observed Hα/Hβ Balmer decrement on the 24 galaxies where it is possible (we use the extinction law of Seaton 1979, and a theoretical Balmer decrement of 2.87 from Osterbrock 1989). The E($B-V$) coefficients that we found are given in Table 7. We then used these results to correct the [OII]λ3727/Hβ flux ratio for reddening and we compared it to the same equivalent width ratio.

Fig. 16 shows the result of this comparison. We see that the equivalent width ratio is consistent with the dust-corrected flux ratio, with the exception of two very high ratios which are underestimated with equivalent widths. The rms of the residuals around the $y = x$ line is 0.10 dex. We conclude that the "blue" diagnostic diagrams are not significantly affected by the differential attenuation between [OII]λ3727 and Hβ emission lines. The low value of the rms of the residuals tells us that any possible effect is already included in the error domain of the "blue" calibration.

7. Conclusions

We have defined a sample of 141 emission-line galaxies at intermediate redshifts ranging from $z = 0.2$ to $z = 1.0$. We obtained medium-resolution spectroscopic observations of these galaxies in the optical range, and associated *R*-band photometry. The following conclusions can be drawn from this paper:

- Our sample has been used to test the `platefit` software originally developed by C. Tremonti, and which is designed to automatically measure spectral features (e.g. emission lines). We managed to adapt it to our lower resolution and SNR spectra. The comparison with manual measurements shows that we get better measurements for those emission lines where Balmer absorption features are important (e.g. Hα, Hβ and [OII]λ3727 emission lines), and that we get correct measurements of flux and equivalent widths for blended lines (e.g. [NII]λ6584 and Hα emission lines).
- We have done as careful a job as possible and are reasonably sure that the `platefit` software can also be used for future and ongoing large surveys (VVDS, zCOSMOS, etc) which are based on low resolution spectroscopy. We verify, by downgrading the resolution of our spectra, that the flux and equivalent-width measurements at low resolution are not altered more than the measurement error. In particular, the [NII]λ6584/Hα line ratio is robust to resolution changes.
- The `platefit` software has been used to measure *k*-corrected spectroscopic colors. Our sample of galaxies covers all the late-type range in a color-color diagram, with a maximum for the Irregular and Sc spectral types.

– Standard and "blue" diagnostic diagrams show a majority of star-forming galaxies, and some narrow-lines AGNs (i.e. Seyfert 2 galaxies), covering the whole range of ionization level and collisional excitation degree. Because the Hα line gets redshifted out of the optical range at high redshifts, $\sim$ 70% of our sample must be classified using the "blue" diagnostic diagrams. About 10% of our galaxies still remain unclassified because they fall in the uncertainty region of these diagrams, we classify them as "candidate" star-forming galaxies.

More analysis in terms of chemical abundances and stellar populations will be described in subsequent papers.

Acknowledgements. We thank C. Tremonti for giving us the right to use the `platefit` software. F.L. would like to thank warmly R. Pelló for decisive help on photometric reduction and AB correction calculations. J.B. acknowledges the receipt of an ESA external postdoctoral fellowship. J.B. acknowledges the receipt of FCT fellowship BPD/14398/2003. We thank N. Courtney for the photometric calibration of the J1206 field and R. Ellis for providing us Keck spectroscopy of some magnified objects. We thank the anonymous referee for useful comments and suggestions.

References

Abazajian, K., Adelman-McCarthy, J. K., Agüeros, M. A., et al. 2004, AJ, 128, 502
Abazajian, K., Adelman-McCarthy, J. K., Agüeros, M. A., et al. 2003, AJ, 126, 2081
Abraham, R. G., Glazebrook, K., McCarthy, P. J., et al. 2004, AJ, 127, 2455
Bertin, E. & Arnouts, S. 1996, A&AS, 117, 393
Brinchmann, J., Abraham, R., Schade, D., et al. 1998, ApJ, 499, 112
Brinchmann, J., Charlot, S., White, S. D. M., et al. 2004, MNRAS, 351, 1151
Bruzual, G. & Charlot, S. 2003, MNRAS, 344, 1000
Campusano, L. E., Pelló, R., Kneib, J.-P., et al. 2001, A&A, 378, 394
Chen, H., McCarthy, P. J., Marzke, R. O., et al. 2002, ApJ, 570, 54
Colless, M., Dalton, G., Maddox, S., et al. 2001, MNRAS, 328, 1039
Contini, T., Treyer, M. A., Sullivan, M., & Ellis, R. S. 2002, MNRAS, 330, 75
Couch, W. J., Balogh, M. L., Bower, R. G., et al. 2001, ApJ, 549, 820
Czoske, O., Kneib, J.-P., & Bardeau, S. 2002, ASP Conf. Series, eds. S. Bowyer & C.-Y. Hwang, (astro-ph/0211517)
Ellis, R., Santos, M. R., Kneib, J., & Kuijken, K. 2001, ApJ, 560, L119
Franx, M., Illingworth, G. D., Kelson, D. D., van Dokkum, P. G., & Tran, K. 1997, ApJ, 486, L75+
Fukugita, M., Ichikawa, T., Gunn, J. E., et al. 1996, AJ, 111, 1748
Guzman, R., Gallego, J., Koo, D. C., et al. 1997, ApJ, 489, 559
Hammer, F., Gruel, N., Thuan, T. X., Flores, H., & Infante, L. 2001, ApJ, 550, 570
Kauffmann, G., Heckman, T. M., Tremonti, C., et al. 2003a, MNRAS, 346, 1055
Kauffmann, G., Heckman, T. M., White, S. D. M., et al. 2003b, MNRAS, 341, 33
Kewley, L. J., Heisler, C. A., Dopita, M. A., & Lumsden, S. 2001, ApJS, 132, 37
Kewley, L. J., Jansen, R. A., & Geller, M. J. 2005, PASP, 117, 227
Kneib, J.-P. 1993, Ph.D. Thesis
Kneib, J.-P., Ellis, R. S., Smail, I., Couch, W. J., & Sharples, R. M. 1996, ApJ, 471, 643
Kobulnicky, H. A., Willmer, C. N. A., Phillips, A. C., et al. 2003, ApJ, 599, 1006
Kobulnicky, H. A. & Zaritsky, D. 1999, ApJ, 511, 118
Koo, D. C. & DEEP Team. 2002, Bulletin of the American Astronomical Society, 34, 1320
Lamareille, F., Mouhcine, M., Contini, T., Lewis, I., & Maddox, S. 2004, MNRAS, 350, 396
Le Borgne, J.-F., Bruzual, G., Pelló, R., et al. 2003, A&A, 402, 433
Le Fèvre, O., Abraham, R., Lilly, S. J., et al. 2000, MNRAS, 311, 565
Le Fèvre, O., Mellier, Y., McCracken, H. J., et al. 2004, A&A, 417, 839
Le Fevre, O., Vettolani, G., Maccagni, D., et al. 2003, in Discoveries and Research Prospects from 6- to 10-Meter-Class Telescopes II. Edited by Guhathakurta, Puragra. Proceedings of the SPIE, Volume 4834, pp. 173-182 (2003)., 173–182
Liang, Y. C., Hammer, F., Flores, H., et al. 2004a, A&A, 423, 867
Liang, Y. C., Hammer, F., Flores, H., Gruel, N., & Assémat, F. 2004b, A&A, 417, 905
Lilly, S., Schade, D., Ellis, R., et al. 1998, ApJ, 500, 75
Lilly, S. J., Carollo, C. M., & Stockton, A. N. 2003, ApJ, 597, 730
Lilly, S. J., Le Fevre, O., Crampton, D., Hammer, F., & Tresse, L. 1995, ApJ, 455, 50
Maier, C., Lilly, S. J., Carollo, M., Stockton, A., & Brodwin, M. 2005, ApJ, in press (astro-ph/0508239)
Maier, C., Meisenheimer, K., & Hippelein, H. 2004, A&A, 418, 475
Natarajan, P., Kneib, J., Smail, I., & Ellis, R. S. 1998, ApJ, 499, 600
Oke, J. B. 1974, ApJS, 27, 21
Oke, J. B., Cohen, J. G., Carr, M., et al. 1995, PASP, 107, 375
Osterbrock, D. E. 1989, Astrophysics of gaseous nebulae and active galactic nuclei (Mill Valley, CA, University Science Books, 1989, 422 p.)
Pelló, R., Kneib, J. P., Le Borgne, J. F., et al. 1999, A&A, 346, 359
Pettini, M. & Pagel, B. E. J. 2004, MNRAS, 348, L59
Santos, M. R., Ellis, R. S., Kneib, J., Richard, J., & Kuijken, K. 2004, ApJ, 606, 683
Schade, D., Lilly, S. J., Crampton, D., et al. 1999, ApJ, 525, 31
Schlegel, D. J., Finkbeiner, D. P., & Davis, M. 1998, ApJ, 500, 525
Seaton, M. J. 1979, MNRAS, 187, 73P

Smail, I., Kuntschner, H., Kodama, T., et al. 2001, MNRAS, 323, 839
Smith, G. P., Edge, A. C., Eke, V. R., et al. 2003, ApJ, 590, L79
Spergel, D. N., Verde, L., Peiris, H. V., et al. 2003, ApJS, 148, 175
Strateva, I., Ivezić, Ž., Knapp, G. R., et al. 2001, AJ, 122, 1861
Tremonti, C. A., Heckman, T. M., Kauffmann, G., et al. 2004, ApJ, 613, 898
van Zee, L., Salzer, J. J., Haynes, M. P., O'Donoghue, A. A., & Balonek, T. J. 1998, AJ, 116, 2805
Veilleux, S. & Osterbrock, D. E. 1987, ApJS, 63, 295

Online Material

Table 6. Photometric data. *LCL05*: identification number, see Tables 1, 2 and 3.R_{AB}: photometric magnitude in the *R* band (or *I* band for filter 5). *filter*: the filter used (1: FORS *R* Gunn, 2: FORS *R* Bessel, 3: TEK2048 *R*, 4: BTC *R*, 5: CFH12k *I*, 6: WFPC *F*606*W*). *ape*: aperture differences (the difference between observed and spectroscopic magnitude in the given filter). I^0_{AB}: *k*-corrected magnitude in the *I* band (the sum of the spectroscopic magnitude in rest-frame and the aperture differences). A_I: foreground dust extinction in the *I* band (rest-frame). $(U-B)^0_{AB}$,$(B-V)^0_{AB}$, $(V-R)^0_{AB}$, $(V-I)^0_{AB}$: foreground-dust- and *k*-corrected spectroscopic colors. $(u-g)^0_{AB}$,$(g-r)^0_{AB}$, $(g-i)^0_{AB}$: foreground-dust- and *k*-corrected spectroscopic colors with the SDSS filters. $M_{AB}(I)$: foreground-dust- and *k*-corrected absolute magnitude in the *I* band. *lens*: lensing correction if necessary (already applied to $M_{AB}(I)$).

LCL05	R_{AB}	filter	ape	I^0_{AB}	A_I	$(U-B)^0_{AB}$	$(B-V)^0_{AB}$	$(V-R)^0_{AB}$	$(V-I)^0_{AB}$	$(u-g)^0_{AB}$	$(g-r)^0_{AB}$	$(g-i)^0_{AB}$	$M_{AB}(I)$	lens
001	21.22	1	−0.56	21.03	0.04	...	0.49	0.17	0.31	0.88	0.31	0.46	−20.26 ± 0.04	0.00
002	21.11	1	−0.54	21.26	0.02	1.01	0.21	0.00	−0.01	0.89	−0.05	−0.07	−21.56 ± 0.04	0.00
003	20.47	1	−0.61	20.37	0.04	1.20	0.31	0.16	0.32	0.68	0.22	0.38	−20.93 ± 0.03	0.00
004	19.92	1	−1.41	19.43	0.04	0.83	0.36	0.28	0.62	...	0.41	0.69	−21.27 ± 0.02	0.00
005	19.19	1	−0.63	18.68	0.04	...	0.89	0.30	0.56	...	0.63	0.92	−22.02 ± 0.01	0.00
006	21.14	1	−0.69	20.96	−0.05	1.14	0.34	0.13	0.26	1.05	0.26	0.37	−19.45 ± 0.04	0.00
007	20.15	1	−0.57	19.85	0.04	0.94	0.58	0.22	0.40	...	0.47	0.65	−20.86 ± 0.02	0.00
008	20.87	1	−0.61	20.71	0.04	...	0.30	0.15	0.32	...	0.30	0.41	−19.76 ± 0.03	0.00
009	20.22	1	−0.59	20.04	0.04	...	0.44	0.16	0.31	...	0.34	0.48	−20.83 ± 0.02	0.00
010	20.88	1	−0.60	20.24	0.04	1.27	0.83	0.38	0.68	1.48	0.74	1.03	−20.45 ± 0.03	0.00
011	20.48	1	−1.09	20.26	0.04	1.21	0.36	0.20	0.38	0.85	0.33	0.49	−20.69 ± 0.03	0.00
012	20.95	1	−0.79	20.54	0.05	3.93	0.83	0.33	0.61	...	0.60	0.91	−17.49 ± 0.04	0.00
013	21.14	1	−1.36	20.80	0.04	2.06	0.56	0.22	0.42	1.14	0.40	0.61	−19.71 ± 0.04	0.00
014	20.61	1	−1.34	19.58	0.04	2.23	0.94	0.46	0.86	1.69	0.77	1.20	−22.07 ± 0.03	0.00
015	22.75	1	−0.13	22.81	0.05	0.80	0.18	0.07	0.16	0.84	0.07	0.14	−17.65 ± 0.10	0.00
016	21.07	1	−0.69	21.47	0.04	0.51	0.16	−0.08	0.04	0.59	−0.07	−0.05	−19.49 ± 0.03	0.00
017	21.01	1	−1.11	20.46	0.04	...	0.79	0.36	0.63	...	0.65	0.96	−20.02 ± 0.04	0.00
018	21.22	1	−0.81	21.01	0.13	...	0.37	0.14	0.27	...	0.28	0.39	−19.10 ± 0.05	0.00
019	22.11	1	−0.65	23.00	0.14	...	...	−0.03	−0.86	...	0.27	−0.24	−16.93 ± 0.12	0.00
020	21.95	1	−0.53	21.53	0.11	...	0.45	0.21	0.40	0.86	0.36	0.57	−20.72 ± 0.10	0.00
021	21.16	1	−0.46	21.00	0.13	...	0.48	0.23	0.37	...	0.23	0.30	−19.71 ± 0.05	0.00
022	21.85	1	−0.40	22.00	0.08	0.60	0.10	0.04	0.08	0.54	0.01	0.05	−20.83 ± 0.09	0.00
023	20.90	1	−0.78	20.60	0.11	1.00	0.36	0.19	0.35	0.76	0.29	0.46	−21.58 ± 0.05	0.00
024	21.72	1	−0.77	21.49	0.05	...	0.26	0.12	0.24	0.61	0.16	0.28	−21.52 ± 0.09	0.00
025	20.73	1	−1.44	20.54	0.15	1.17	0.29	0.15	0.29	0.86	0.22	0.37	−19.76 ± 0.06	0.00
026	21.63	1	−0.87	21.19	0.15	...	1.36	0.59	0.84	...	0.10	0.36	−19.11 ± 0.08	0.00
027	22.42	1	−0.85	22.37	0.13	1.13	0.31	0.01	0.13	...	0.16	0.17	−17.91 ± 0.12	0.00
028	19.76	1	−0.82	19.55	0.15	1.83	0.41	0.17	0.30	1.46	0.33	0.45	−20.21 ± 0.02	0.00
029	21.13	1	−1.16	20.50	0.10	1.21	0.50	0.27	0.53	0.96	0.42	0.69	−21.92 ± 0.06	0.00
030	22.24	1	−0.66	22.16	0.08	1.04	0.21	0.09	0.18	0.65	0.15	0.25	−20.69 ± 0.13	0.00
031	22.32	1	−0.36	22.07	0.14	...	0.34	0.13	0.30	...	0.29	0.39	−18.23 ± 0.12	0.00
032	22.00	1	0.09	21.55	0.07	...	0.38	0.29	0.51	...	−0.17	0.60	−20.61 ± 0.06	0.00
033	21.33	1	−0.19	20.91	0.08	1.56	0.66	0.25	0.43	1.21	0.54	0.72	−20.06 ± 0.03	0.00
034	21.16	1	−0.47	21.13	0.08	...	0.53	0.24	0.31	0.73	0.07	0.14	−20.04 ± 0.03	0.00
035	21.16	1	−0.50	21.03	0.09	1.50	0.26	0.17	0.30	0.80	0.21	0.35	−19.92 ± 0.03	0.00
036	21.05	1	0.24	20.89	0.10	1.22	0.24	0.11	0.25	0.86	0.31	0.31	−19.26 ± 0.02	0.00
037	20.61	1	−0.39	19.71	0.08	...	0.49	0.56	0.97	...	0.00	1.03	−22.16 ± 0.03	0.00
038	20.37	1	−0.08	20.21	0.10	...	...	0.10	0.29	...	0.23	0.32	−20.18 ± 0.02	0.00
039	20.45	1	−0.57	20.31	0.08	1.24	0.36	0.14	0.27	1.07	0.26	0.38	−20.65 ± 0.02	0.00
040	21.51	1	−0.49	21.59	0.06	1.19	0.18	0.08	0.16	0.53	0.07	0.15	−20.92 ± 0.04	0.00
041	20.66	1	−2.75	20.13	0.09	2.20	0.60	0.39	0.69	1.82	0.34	0.87	−20.09 ± 0.03	0.00
042	22.17	1	−1.05	22.28	0.08	1.07	0.18	0.10	0.21	0.45	0.07	0.18	−19.15 ± 0.08	0.00
043	22.49	1	−0.46	21.92	0.09	0.77	0.56	0.27	0.57	...	0.49	0.78	−19.30 ± 0.09	0.00
044	20.44	1	−0.65	20.08	0.10	1.48	0.54	0.21	0.41	0.98	0.40	0.61	−20.75 ± 0.02	0.00
045	21.77	1	−0.43	21.34	0.07	0.82	0.10	0.26	0.63	0.50	−0.12	0.25	−20.82 ± 0.04	0.00
046	22.26	1	−0.20	21.65	0.04	1.24	0.45	0.21	0.41	0.87	0.36	0.56	−21.34 ± 0.08	0.00
047	23.42	1	−0.39	22.95	0.07	0.96	0.28	0.27	0.59	0.56	0.30	0.64	−19.23 ± 0.25	0.00
048	22.11	1	−1.07	21.97	0.09	0.97	0.29	0.11	0.29	0.74	0.26	0.35	−19.02 ± 0.08	0.00
049	20.62	1	−0.53	20.11	0.10	...	0.60	0.30	0.59	...	0.56	0.81	−20.27 ± 0.02	0.00
050	22.15	1	−0.65	21.25	0.05	1.19	0.56	0.37	0.72	0.86	0.49	0.87	−21.24 ± 0.09	0.00
051	21.66	1	−0.56	21.74	0.08	...	0.32	0.13	0.26	0.49	−0.01	0.13	−19.91 ± 0.05	0.00
052	21.57	1	−0.14	21.77	0.08	0.95	0.36	−0.01	0.11	0.58	0.02	0.14	−19.08 ± 0.07	0.00
053	20.93	1	−0.25	20.99	0.05	1.28	0.22	0.08	0.16	0.64	0.14	0.21	−21.51 ± 0.05	0.00
054	20.88	1	−0.36	21.17	0.05	1.17	0.11	0.01	0.05	0.65	0.02	0.05	−21.35 ± 0.03	0.00
055	20.23	1	−0.35	19.32	0.06	...	0.97	0.33	0.64	1.24	0.60	0.93	−22.82 ± 0.02	0.00
056	19.89	1	−0.59	19.24	0.08	1.70	0.78	0.37	0.67	1.39	0.64	0.96	−21.60 ± 0.02	0.00
057	19.67	1	−0.19	18.82	0.08	...	0.94	0.47	0.81	1.60	0.75	1.13	−22.46 ± 0.01	0.00
058	21.30	1	−0.96	21.86	0.07	0.35	−0.34	−0.21	−0.41	...	−0.49	−0.71	−19.09 ± 0.05	0.00
059	20.71	1	−0.69	20.33	0.09	1.80	0.40	0.22	0.52	0.97	0.28	0.57	−20.50 ± 0.04	0.00
060	21.79	1	−0.11	21.74	0.08	1.00	0.18	0.18	0.31	0.74	0.18	0.31	−19.73 ± 0.07	0.00
061	21.11	1	−0.15	20.67	0.08	0.73	0.40	0.29	0.58	0.88	0.21	0.67	−20.80 ± 0.04	0.00
062	21.08	1	−0.13	20.70	0.08	1.13	0.52	0.24	0.45	1.00	0.46	0.66	−20.19 ± 0.04	0.00
063	21.59	1	−0.18	21.37	0.08	...	0.13	0.33	0.51	...	−0.31	0.43	−19.51 ± 0.05	0.00
064	20.56	2	−0.77	19.60	0.15	1.90	0.99	0.53	0.98	1.35	0.81	1.31	−20.95 ± 0.01	0.00
065	21.88	2	−0.76	21.64	0.21	0.92	0.45	−0.10	0.07	0.46	0.14	0.07	−15.93 ± 0.03	0.00
066	23.42	2	−1.02	22.76	0.13	...	...	0.14	0.54	0.56	−0.06	0.29	−19.19 ± 0.15	0.01
067	22.48	2	−0.71	22.92	0.11	1.60	0.13	−0.07	−0.15	0.86	−0.18	−0.27	−19.16 ± 0.07	0.01
068	22.95	2	−0.91	22.37	0.05	1.13	0.30	0.19	0.50	0.74	0.15	0.44	−20.51 ± 0.13	0.03
069	21.42	2	−1.68	21.23	0.17	1.59	0.42	0.15	0.27	0.73	0.31	0.36	−19.12 ± 0.03	0.00
070	22.73	2	−0.06	21.73	0.03	1.13	0.36	0.29	0.78	0.58	0.30	0.77	−21.53 ± 0.12	0.06
071	21.72	2	−0.90	21.64	0.10	0.91	0.19	0.12	0.23	0.51	0.11	0.23	−20.70 ± 0.03	0.15
072	21.99	2	−0.98	21.82	0.13	1.53	0.38	0.13	0.25	0.85	0.21	0.34	−19.55 ± 0.03	0.04
073	20.59	2	−0.94	20.49	0.02	...	0.40	0.12	0.28	...	0.31	0.43	−20.12 ± 0.01	0.00

Table 6. continued.

LCL05	R_{AB}	filter	ape	I^0_{AB}	A_I	$(U-B)^0_{AB}$	$(B-V)^0_{AB}$	$(V-R)^0_{AB}$	$(V-I)^0_{AB}$	$(u-g)^0_{AB}$	$(g-r)^0_{AB}$	$(g-i)^0_{AB}$	$M_{AB}(I)$	lens
074	19.21	2	−2.03	19.20	0.03	...	...	0.53	0.61	...	0.13	−0.04	−19.03 ± 0.00	0.00
075	20.34	2	−1.53	20.26	0.03	...	...	0.07	0.21	...	0.22	0.16	−18.02 ± 0.01	0.00
076	20.15	2	−0.68	20.05	0.02	1.26	0.40	0.13	0.28	...	0.28	0.43	−21.08 ± 0.01	0.00
077	20.28	2	−0.49	20.20	0.02	...	0.54	0.22	0.35	1.86	0.26	0.39	−20.76 ± 0.01	0.00
078	20.92	2	−1.16	20.39	0.01	1.16	0.51	0.24	0.46	1.09	0.40	0.63	−21.93 ± 0.01	0.27
079	21.79	2	−0.93	21.32	0.02	1.44	0.60	0.28	0.52	1.16	0.47	0.74	−20.28 ± 0.02	0.16
080	21.19	2	−0.90	21.22	0.02	...	0.85	0.22	0.32	1.17	0.18	0.28	−19.99 ± 0.01	0.00
081	23.47	2	−0.28	23.29	0.02	0.70	0.27	0.24	0.43	0.79	0.17	0.46	−18.23 ± 0.05	0.04
082	20.25	2	−0.97	19.55	0.02	...	0.85	0.35	0.64	1.44	0.63	0.96	−22.15 ± 0.01	0.06
083	22.64	2	−0.40	22.81	0.01	0.89	0.07	0.05	0.18	0.33	0.05	0.15	−20.30 ± 0.03	0.14
084	22.26	2	−0.67	21.83	0.02	1.25	0.59	0.23	0.47	0.95	0.45	0.71	−19.89 ± 0.04	0.03
085	23.20	2	−0.72	23.02	0.01	1.27	0.30	0.12	0.23	0.64	0.20	0.32	−20.12 ± 0.05	0.09
086	22.58	2	−0.73	22.37	0.02	−2.15	−0.92	0.19	0.34	0.92	0.32	0.48	−19.36 ± 0.07	0.04
087	22.75	2	−0.96	22.64	0.02	0.90	0.63	−0.10	0.09	0.61	0.21	0.41	−19.03 ± 0.04	0.07
088	23.22	2	−0.62	23.39	0.00	0.97	0.10	0.04	0.09	0.43	0.06	0.11	−19.97 ± 0.09	0.00
089	22.14	2	−0.70	21.87	0.04	1.14	0.41	0.15	0.27	0.83	0.24	0.37	−20.70 ± 0.03	0.04
090	22.37	2	−0.88	21.91	0.04	1.07	0.43	0.23	0.44	0.80	0.30	0.53	−20.68 ± 0.04	0.03
091	22.30	2	−0.87	21.77	0.04	...	2.14	0.05	0.12	0.72	0.11	0.17	−21.66 ± 0.04	0.07
092	22.53	2	−0.60	22.52	0.08	1.32	0.06	0.08	0.24	0.46	−0.10	0.05	−18.73 ± 0.04	0.00
093	22.15	2	−1.05	21.96	0.03	1.20	0.21	0.14	0.34	0.46	0.17	0.36	−20.87 ± 0.03	0.10
094	23.63	2	−0.30	23.60	0.06	1.28	0.23	0.11	0.20	0.48	0.16	0.27	−19.00 ± 0.11	0.05
095	22.91	2	−0.48	22.36	0.08	1.75	0.44	0.30	0.67	0.93	0.35	0.73	−18.98 ± 0.07	0.01
096	22.05	2	−1.00	21.73	0.06	1.17	0.44	0.18	0.37	0.80	0.32	0.53	−20.17 ± 0.04	0.08
097	21.41	2	−2.11	21.00	0.03	1.33	0.42	0.20	0.38	0.73	0.31	0.51	−21.39 ± 0.03	0.25
098	24.29	2	0.01	23.95	0.05	1.19	0.38	0.20	0.39	0.71	0.26	0.47	−18.39 ± 0.12	0.31
099	21.05	3	−0.91	21.19	0.07	0.88	0.13	0.16	0.19	0.87	0.07	0.10	−20.25 ± 0.02	0.00
100	21.36	3	−1.08	21.54	0.07	...	0.40	0.04	0.10	0.78	0.01	0.06	−19.89 ± 0.03	0.00
101	20.95	3	−1.58	20.60	0.08	...	0.94	0.21	0.40	1.01	0.35	0.56	−20.85 ± 0.02	0.00
102	20.30	3	−1.17	19.42	0.07	...	0.84	0.34	0.65	1.52	0.65	0.98	−22.50 ± 0.01	0.00
103	20.43	3	−1.32	20.23	0.06	...	0.42	0.14	0.28	0.89	0.22	0.37	−21.96 ± 0.02	0.00
104	21.49	3	−1.00	21.02	0.07	1.91	0.63	0.21	0.38	1.29	0.41	0.59	−21.04 ± 0.02	0.00
105	21.85	5	0.40	20.48	0.01	1.72	1.15	0.63	1.19	1.86	1.03	1.64	−23.13 ± 0.01	0.00
106	23.02	5	−0.69	22.20	0.01	0.69	0.62	0.49	1.08	0.90	0.48	1.08	−21.40 ± 0.03	0.00
107	24.02	5	0.26	22.88	0.00	0.46	0.85	0.58	1.10	1.09	0.56	1.14	−20.84 ± 0.06	0.00
108	23.19	5	0.70	21.71	0.01	1.69	1.30	0.69	1.28	2.13	1.15	1.81	−21.76 ± 0.03	0.00
109	24.04	5	0.87	24.49	0.00	0.40	−0.12	0.13	0.32	0.87	−0.73	−0.55	−19.37 ± 0.05	0.00
110	21.40	5	0.59	20.45	0.00	1.63	0.77	0.40	0.79	1.55	0.64	1.06	−23.65 ± 0.01	0.00
111	21.63	4	−0.86	19.88	0.01	1.60	0.91	0.46	0.86	...	0.80	1.24	−23.19 ± 0.01	0.00
112	22.10	4	0.41	20.30	0.01	...	0.99	0.56	1.08	...	0.92	1.48	−22.50 ± 0.01	0.00
113	23.47	4	0.03	22.00	0.00	0.85	0.49	0.39	0.83	0.81	0.53	0.99	−22.00 ± 0.02	0.00
114	23.69	4	0.39	21.25	0.00	1.38	1.03	0.58	1.09	1.64	0.89	1.46	−22.40 ± 0.02	0.00
115	21.45	4	−0.51	19.60	0.01	...	1.11	0.52	0.98	...	0.92	1.42	−23.20 ± 0.00	0.00
116	21.00	4	−0.49	19.30	0.01	1.58	1.02	0.47	0.90	...	0.85	1.31	−23.51 ± 0.00	0.00
117	22.11	4	−0.15	20.38	0.01	1.18	1.06	0.58	1.07	...	0.96	1.52	−22.22 ± 0.01	0.00
118	22.69	4	0.29	21.81	0.01	0.94	0.58	0.34	0.67	...	0.54	0.89	−20.79 ± 0.01	0.00
119	23.11	4	0.06	21.34	0.01	1.19	0.80	0.45	0.86	1.33	0.73	1.18	−22.14 ± 0.01	0.00
120	23.76	4	−1.01	23.23	0.01	0.57	0.39	0.23	0.45	0.82	0.28	0.51	−19.79 ± 0.02	0.00
122	23.15	5	0.55	23.51	0.01	0.76	0.17	0.09	0.17	0.75	0.06	0.15	−20.06 ± 0.04	0.00
123	23.22	5	0.23	23.25	0.02	0.74	0.33	0.19	0.36	0.84	0.25	0.43	−20.12 ± 0.04	0.00
124	22.41	5	0.13	22.51	0.02	0.75	0.29	0.16	0.30	...	0.25	0.40	−20.96 ± 0.02	0.00
125	23.45	5	−0.18	22.79	0.02	0.93	0.73	0.44	0.85	1.21	0.66	1.11	−20.27 ± 0.05	0.00
126	22.37	5	0.51	22.02	0.02	0.85	0.56	0.31	0.60	1.02	0.49	0.80	−21.34 ± 0.02	0.00
127	23.17	5	−0.27	22.93	0.02	0.89	0.44	0.27	0.55	1.00	0.31	0.60	−20.55 ± 0.04	0.00
128	22.78	5	0.41	22.66	0.06	...	...	0.26	0.50	...	0.41	0.66	−19.49 ± 0.03	0.00
129	23.38	5	−0.27	23.22	0.01	0.61	0.41	0.27	0.55	0.90	0.21	0.50	−20.26 ± 0.05	0.00
130	24.19	5	0.04	24.14	0.05	...	0.44	0.17	0.43	...	0.85	0.59	−18.00 ± 0.08	0.00
131	23.92	5	−0.02	24.41	0.01	0.50	−0.03	0.06	0.15	0.67	−0.32	−0.24	−19.35 ± 0.07	0.00
132	23.78	5	0.11	23.66	0.04	0.73	0.42	0.26	0.51	...	0.36	0.62	−19.23 ± 0.06	0.00
133	23.77	5	0.10	23.78	0.06	...	0.31	0.09	0.37	...	0.85	0.54	−18.38 ± 0.06	0.00
134	22.22	5	−0.25	21.80	0.03	...	0.65	0.36	0.69	...	0.62	0.98	−21.03 ± 0.02	0.00
135	22.18	5	0.52	21.04	0.01	0.82	0.81	0.54	1.02	0.97	0.82	1.36	−22.75 ± 0.02	0.00
136	19.82	5	−0.62	19.50	0.01	1.13	0.72	0.31	0.58	1.26	0.58	0.87	−22.21 ± 0.01	1.42
137	20.32	5	−0.51	20.41	0.03	0.68	0.27	0.16	0.31	0.76	0.22	0.38	−20.20 ± 0.03	1.53
138	22.43	5	0.99	21.85	0.03	0.64	0.61	0.50	1.10	...	0.60	1.21	−19.48 ± 0.16	0.67
139	21.18	5	−0.37	21.63	0.01	0.42	0.16	0.07	0.14	0.40	0.16	0.22	−19.99 ± 0.01	1.65
140	21.41	5	−0.79	21.45	0.01	0.85	0.52	0.19	0.35	0.98	0.38	0.55	−20.47 ± 0.03	1.35
141	21.14	5	−0.36	21.02	0.03	0.67	0.36	0.26	0.62	...	0.36	0.73	−20.07 ± 0.01	0.60
142	23.40	6	−0.45	22.11	0.03	0.35	0.87	0.21	0.77	...	0.46	1.06	−19.31 ± 0.03	0.33

Table 7. Spectral classification.*LCL05*: identification number, see Tables 1,2 and 3. *Standard*: standard diagnostic. *Blue*: "blue" diagnostic (see text for details). *Type*: final spectral type. *E(B − V)*: extinction coefficient computed from Hα/Hβ ratio.

LCL05	Standard	Blue	Type	E($B-V$)
001	...	SF	Star-forming	...
002	...	SF	Star-forming	...
003	...	SF	Star-forming	...
004	SF	SF	Star-forming	0.32 ± 0.02
005	Sey2	*undef*	Seyfert 2	...
006	SF	SF	Star-forming	0.06 ± 0.04
007	SF	SF	Star-forming	1.06 ± 0.09
008	SF	SF	Star-forming	0.05 ± 0.02
009	SF	SF	Star-forming	0.01 ± 0.04
010	SF	SF	Star-forming	0.83 ± 0.05
011	SF	SF	Star-forming	0.66 ± 0.05
012	SF	...	Star-forming	...
013	...	SF	Star-forming	...
014	...	SF	Star-forming	...
015	SF	SF	Star-forming	0.12 ± 0.04
016	SF	*undef*	Star-forming	0.19 ± 0.01
017	Sey2	Sey2	Seyfert 2	0.61 ± 0.55
018	...	*undef*	*Star-forming ?*	...
019	SF	...	Star-forming	0.04 ± 0.02
020	...	SF	Star-forming	...
021	SF	SF	Star-forming	0.15 ± 0.02
022	...	SF	Star-forming	...
023	...	SF	Star-forming	...
024	...	SF	Star-forming	...
025	...	*undef*	*Star-forming ?*	...
026	...	SF	Star-forming	...
027	...	*undef*	*Star-forming ?*	...
028	SF	SF	Star-forming	0.28 ± 0.01
029	...	SF	Star-forming	...
030	...	SF	Star-forming	...
031	SF	*undef*	Star-forming	0.25 ± 0.03
032	...	SF	Star-forming	...
033	SF	...	Star-forming	0.97 ± 0.07
034	SF	SF	Star-forming	0.10 ± 0.03
035	...	SF	Star-forming	...
036	SF	SF	Star-forming	0.27 ± 0.01
037	...	*undef*	*Star-forming ?*	...
038	SF	SF	Star-forming	0.01 ± 0.01
039	SF	SF	Star-forming	0.14 ± 0.02
040	...	SF	Star-forming	...
041	...	SF	Star-forming	...
042	...	SF	Star-forming	...
043	...	SF	Star-forming	...
044	...	SF	Star-forming	...
045	...	*undef*	*Star-forming ?*	...
046	...	SF	Star-forming	...
047	...	SF	Star-forming	...
048	...	...	*undef*	...
049	SF	SF	Star-forming	0.55 ± 0.02
050	...	SF	Star-forming	...
051	...	*undef*	*Star-forming ?*	...
052	SF	SF	Star-forming	0.10 ± 0.01
053	...	SF	Star-forming	...
054	...	SF	Star-forming	...
055	...	SF	Star-forming	...
056	SF	SF	Star-forming	0.45 ± 0.03
057	...	SF	Star-forming	...
058	...	SF	Star-forming	...
059	...	SF	Star-forming	...
060	...	SF	Star-forming	...
061	...	SF	Star-forming	...
062	SF	SF	Star-forming	0.29 ± 0.02
063	...	SF	Star-forming	...
064	Sey2	*undef*	Seyfert 2	0.76 ± 0.01
065	SF	*undef*	Star-forming	0.23 ± 0.00
066	...	SF	Star-forming	...
067	...	SF	Star-forming	...
068	...	SF	Star-forming	...
069	SF	SF	Star-forming	0.14 ± 0.03
070	...	SF	Star-forming	...
071	...	SF	Star-forming	...
072	...	SF	Star-forming	...
073	SF	SF	Star-forming	0.27 ± 0.01
074	SF	...	Star-forming	0.09 ± 0.00
075	SF	...	Star-forming	0.03 ± 0.02
076	SF	SF	Star-forming	0.55 ± 0.02
077	SF	SF	Star-forming	0.16 ± 0.01
078	...	SF	Star-forming	...
079	...	SF	Star-forming	...
080	SF	SF	Star-forming	...
081	...	SF	Star-forming	...

Table 7. continued

LCL05	Standard	Blue	Type	E($B-V$)
082	...	...	*undef*	...
083	...	SF	Star-forming	...
084	SF	*undef*	Star-forming	0.36 ± 0.04
085	...	*undef*	*Star-forming ?*	...
086	...	SF	Star-forming	...
087	...	SF	Star-forming	...
088	...	*undef*	*Star-forming ?*	...
089	...	*undef*	*Star-forming ?*	...
090	...	*undef*	*Star-forming ?*	...
091	...	SF	Star-forming	...
092	...	*undef*	*Star-forming ?*	...
093	...	SF	Star-forming	...
094	...	...	*undef*	...
095	...	SF	Star-forming	...
096	...	SF	Star-forming	...
097	...	Sey2	Seyfert 2	...
098	...	SF	Star-forming	...
099	...	SF	Star-forming	...
100	...	SF	Star-forming	...
101	...	SF	Star-forming	...
102	...	SF	Star-forming	...
103	...	SF	Star-forming	...
104	...	SF	Star-forming	...
105	...	*undef*	*Star-forming ?*	...
106	...	SF	Star-forming	...
107	...	SF	Star-forming	...
108	...	SF	Star-forming	...
109	...	*undef*	*Star-forming ?*	...
110	...	SF	Star-forming	...
111	...	*undef*	*Star-forming ?*	...
112	...	SF	Star-forming	...
113	...	SF	Star-forming	...
114	...	SF	Star-forming	...
115	...	Sey2	Seyfert 2	...
116	...	SF	Star-forming	...
117	...	SF	Star-forming	...
118	...	SF	Star-forming	...
119	...	SF	Star-forming	...
120	...	SF	Star-forming	...
122	...	SF	Star-forming	...
123	...	SF	Star-forming	...
124	...	SF	Star-forming	...
125	...	SF	Star-forming	...
126	...	SF	Star-forming	...
127	...	SF	Star-forming	...
128	...	SF	Star-forming	...
129	...	SF	Star-forming	...
130	...	Sey2	Seyfert 2	...
131	...	SF	Star-forming	...
132	...	SF	Star-forming	...
133	SF	SF	Star-forming	0.47 ± 0.04
134	...	SF	Star-forming	...
135	...	SF	Star-forming	...
136	...	SF	Star-forming	...
137	...	SF	Star-forming	...
138	...	SF	Star-forming	...
139	...	Sey2	Seyfert 2	...
140	...	*undef*	*Star-forming ?*	...
141	SF	*undef*	Star-forming	1.46 ± 0.21
142	...	*undef*	*Star-forming ?*	0.25 ± 0.04

Table 8. Measurements of forbidden emission lines. Fluxes are given in $f(H\beta)$ units, associated errors in $\sigma[f(H\beta)]$ units. Equivalent widths are given in Å.

	[Oii]λ3727		[Oiii]λ4959		[Oiii]λ5007		[Nii]λ6584		[Sii]$\lambda\lambda$6717+6731	
LCL05	flux	EW	flux	EW	flux	EW	flux	EW	flux	EW
001	2.03 ± 1.0	−23.6 ± 1.7	0.32 ± 0.7	−2.6 ± 1.1	0.31 ± 0.7	−2.7 ± 1.1	...	...	...	...
002	0.79 ± 0.4	−12.4 ± 1.1	...	−0.3 ± 1.4	0.25 ± 0.5	−3.1 ± 1.2	...	...	...	...
003	2.87 ± 1.1	−50.0 ± 0.8	0.59 ± 0.8	−8.9 ± 0.6	1.86 ± 0.9	−29.0 ± 0.7	...	...	...	...
004	2.49 ± 1.6	−20.5 ± 1.0	...	−0.7 ± 1.3	0.16 ± 1.2	−1.0 ± 0.9	0.91 ± 2.9	−6.9 ± 1.6	1.50 ± 2.8	−13.3 ± 2.0
005	1.70 ± 1.4	−3.8 ± 0.6	0.25 ± 1.4	−0.2 ± 0.4	5.86 ± 1.6	−5.5 ± 0.3	2.86 ± 3.4	−3.0 ± 0.5	3.30 ± 3.0	−3.9 ± 0.7
006	3.28 ± 1.6	−28.5 ± 1.7	0.66 ± 1.0	−5.3 ± 1.2	2.20 ± 1.3	−17.6 ± 1.3	...	−1.3 ± 2.7	1.01 ± 3.7	−14.3 ± 6.8
007	3.73 ± 1.5	−7.2 ± 0.9	...	...	0.48 ± 1.3	−0.6 ± 0.7	2.80 ± 2.7	−4.4 ± 1.4	1.63 ± 2.8	−2.9 ± 1.6
008	3.91 ± 1.8	−36.3 ± 1.3	0.55 ± 1.1	−4.7 ± 0.9	1.19 ± 1.2	−10.4 ± 1.0	0.56 ± 1.6	−6.7 ± 1.7	0.96 ± 3.7	−11.3 ± 4.2
009	2.13 ± 1.2	−15.7 ± 1.0	0.21 ± 0.8	−1.1 ± 0.7	0.50 ± 0.8	−2.5 ± 0.6	0.84 ± 1.5	−6.5 ± 1.7	1.48 ± 2.9	−12.4 ± 2.7
010	2.10 ± 1.4	−17.4 ± 2.0	...	−0.2 ± 1.5	0.77 ± 1.1	−3.0 ± 1.1	2.70 ± 2.8	−10.1 ± 2.1	1.60 ± 3.1	−6.1 ± 2.0
011	6.00 ± 1.0	−34.8 ± 0.9	0.62 ± 1.0	−2.8 ± 0.8	1.63 ± 1.0	−7.5 ± 0.8	0.84 ± 2.0	−5.2 ± 2.1	2.24 ± 4.7	−14.6 ± 4.5
012	...	...	−0.40 ± 1.2	1.1 ± 1.1	0.85 ± 1.3	−2.2 ± 1.1	0.24 ± 1.2	−0.7 ± 1.2	2.81 ± 3.4	−7.6 ± 2.5
013	2.92 ± 0.9	−18.2 ± 1.7	0.24 ± 0.8	−1.1 ± 1.6	0.44 ± 0.7	−2.0 ± 1.2	...	...	...	...
014	1.09 ± 0.8	−10.7 ± 1.5	0.29 ± 0.8	−1.2 ± 0.8	0.28 ± 0.7	−1.2 ± 0.7	...	...	...	...
015	2.82 ± 1.4	−30.4 ± 2.2	1.03 ± 1.1	−9.6 ± 1.7	3.34 ± 1.3	−31.3 ± 1.8	0.37 ± 1.8	−6.0 ± 4.5	...	...
016	2.49 ± 1.1	−65.9 ± 0.8	1.69 ± 1.1	−47.3 ± 1.1	5.09 ± 1.2	−147.0 ± 0.9	...	−6.8 ± 2.9	...	−26.9 ± 8.7
017	7.55 ± 1.5	−5.2 ± 2.1	3.14 ± 1.1	−1.0 ± 0.8	−1.84 ± 1.1	0.6 ± 1.1	...	...	12.56 ± 5.0	−4.4 ± 3.4
018	5.09 ± 0.9	−49.7 ± 1.8	0.81 ± 0.7	−5.7 ± 1.2	2.94 ± 0.7	−20.8 ± 1.1	...	...	...	...
019	...	...	0.78 ± 1.1	−12.9 ± 1.7	2.43 ± 1.2	−40.1 ± 1.6	...	...	0.82 ± 3.0	−22.3 ± 6.3
020	2.91 ± 0.6	−27.6 ± 2.7	0.27 ± 0.8	−2.0 ± 2.5	1.12 ± 0.6	−8.2 ± 2.2	...	...	...	...
021	3.33 ± 1.4	−50.5 ± 1.1	0.59 ± 1.2	−8.0 ± 1.1	1.78 ± 1.1	−25.0 ± 1.0	...	...	0.64 ± 2.9	−14.0 ± 3.5
022	2.88 ± 0.6	−48.6 ± 1.1	0.58 ± 0.8	−10.0 ± 2.1	1.71 ± 0.7	−28.9 ± 1.7	...	...	...	...
023	2.25 ± 1.1	−31.7 ± 1.0	0.31 ± 1.1	−3.8 ± 1.1	0.96 ± 1.1	−11.5 ± 1.1	...	...	...	...
024	2.42 ± 0.8	−66.0 ± 1.7	0.40 ± 0.9	−9.0 ± 2.2	1.69 ± 1.1	−40.6 ± 3.7	...	...	...	...
025	6.35 ± 1.6	−34.7 ± 1.9	0.82 ± 0.9	−4.5 ± 1.3	3.51 ± 1.0	−19.3 ± 1.3	...	...	...	...
026	3.09 ± 1.2	−47.7 ± 2.0	0.89 ± 0.8	−12.9 ± 1.3	2.68 ± 0.9	−40.2 ± 1.4	...	...	...	...
027	2.09 ± 1.2	−51.8 ± 4.6	1.14 ± 0.8	−23.0 ± 2.8	4.05 ± 1.0	−84.0 ± 2.7	...	...	...	...
028	3.77 ± 2.3	−30.4 ± 0.7	0.38 ± 1.0	−2.4 ± 0.3	1.00 ± 1.5	−6.5 ± 0.4	1.02 ± 2.1	−9.6 ± 0.8	1.15 ± 2.8	−10.8 ± 1.1
029	3.67 ± 1.1	−21.9 ± 2.1	0.43 ± 1.3	−1.8 ± 1.8	1.36 ± 1.0	−5.6 ± 1.8	...	...	...	...
030	2.40 ± 0.5	−32.8 ± 2.7	0.69 ± 0.6	−9.5 ± 5.3	0.90 ± 0.6	−12.0 ± 4.2	...	...	...	...
031	3.31 ± 1.5	−50.2 ± 2.6	1.52 ± 1.0	−19.8 ± 1.7	4.58 ± 1.1	−59.2 ± 1.6	...	−2.1 ± 3.7	0.57 ± 2.5	−10.2 ± 5.3
032	2.27 ± 1.1	−20.8 ± 1.3	...	0.5 ± 1.6	0.47 ± 1.3	−3.3 ± 1.8	...	...	...	...
033	...	...	...	0.1 ± 0.7	0.58 ± 0.9	−1.3 ± 0.8	2.23 ± 1.5	−6.3 ± 1.1	0.20 ± 1.8	−0.6 ± 1.6
034	4.16 ± 1.3	−45.8 ± 1.1	0.70 ± 1.0	−5.8 ± 0.8	1.88 ± 1.1	−16.3 ± 0.8	...	−4.4 ± 3.4	...	...
035	2.54 ± 1.2	−31.0 ± 1.1	0.25 ± 0.8	−2.8 ± 0.8	0.58 ± 0.9	−6.5 ± 0.9	...	...	...	...
036	4.78 ± 1.5	−50.0 ± 0.6	0.69 ± 0.8	−8.5 ± 0.5	2.19 ± 0.9	−27.6 ± 0.5	0.72 ± 2.0	−11.5 ± 1.3	0.93 ± 1.9	−17.8 ± 1.4
037	3.54 ± 1.0	−22.6 ± 0.9	1.97 ± 1.0	−7.2 ± 0.5	6.01 ± 1.2	−22.1 ± 0.5	...	...	...	...
038	4.20 ± 1.6	−37.5 ± 0.5	0.51 ± 0.9	−4.9 ± 0.4	1.71 ± 1.0	−16.5 ± 0.4	0.38 ± 1.7	−5.9 ± 1.0	1.17 ± 3.8	−18.0 ± 2.3
039	2.38 ± 1.1	−26.3 ± 0.9	0.16 ± 0.9	−1.1 ± 0.6	0.82 ± 1.0	−5.6 ± 0.6	0.78 ± 2.1	−9.1 ± 1.6	1.53 ± 2.6	−18.4 ± 3.0
040	2.41 ± 0.7	−54.3 ± 1.2	0.11 ± 0.6	−2.6 ± 1.7	1.26 ± 0.8	−30.7 ± 1.6	...	...	...	...
041	2.45 ± 1.0	−122.6 ± 11.1	0.28 ± 0.7	−4.1 ± 2.6	1.34 ± 0.7	−18.4 ± 2.3	...	...	...	...
042	2.68 ± 0.9	−55.5 ± 1.8	0.70 ± 0.8	−16.5 ± 2.1	2.34 ± 0.9	−54.1 ± 2.4	...	...	...	...
043	2.18 ± 0.9	−24.7 ± 2.2	0.15 ± 0.8	−1.1 ± 1.5	0.43 ± 0.7	−3.3 ± 1.4	...	...	...	...
044	1.49 ± 0.9	−9.6 ± 0.7	0.09 ± 0.8	−0.4 ± 0.5	0.47 ± 0.7	−2.1 ± 0.5	...	...	...	...
045	1.78 ± 1.0	−83.9 ± 1.0	1.85 ± 1.4	−112.8 ± 2.0	5.41 ± 1.3	−343.3 ± 1.6	...	...	...	...
046	1.36 ± 0.6	−30.1 ± 1.3	...	−1.0 ± 1.5	0.75 ± 1.2	−12.2 ± 2.5	...	...	...	...
047	3.34 ± 1.0	−54.2 ± 3.3	0.60 ± 1.6	−9.8 ± 5.6	2.04 ± 1.2	−33.8 ± 4.6	...	...	...	...
048	191.25 ± 1.2	−44.7 ± 3.2	20.49 ± 1.0	−4.4 ± 2.8	100.59 ± 1.0	−21.9 ± 2.8	...	...	...	...
049	1.49 ± 1.3	−13.0 ± 0.9	...	−0.2 ± 0.5	0.33 ± 1.0	−1.9 ± 0.5	2.12 ± 1.8	−13.5 ± 0.8	2.02 ± 3.1	−12.9 ± 1.8
050	1.87 ± 0.8	−66.6 ± 2.1	0.27 ± 0.8	−8.3 ± 2.2	1.45 ± 1.1	−43.0 ± 3.5	...	...	...	...
051	2.25 ± 1.0	−79.8 ± 1.1	1.15 ± 1.2	−48.8 ± 1.7	3.49 ± 1.1	−147.1 ± 1.3	...	...	...	...
052	2.11 ± 1.2	−72.0 ± 1.1	1.08 ± 1.0	−36.9 ± 1.4	3.25 ± 1.2	−111.5 ± 1.0	1.05 ± 2.7	−72.1 ± 5.6	...	...
053	2.44 ± 0.7	−43.0 ± 0.8	−0.16 ± 0.7	2.6 ± 0.8	1.24 ± 0.8	−19.7 ± 1.4	...	...	...	...
054	2.45 ± 1.0	−35.3 ± 0.7	...	0.2 ± 0.8	1.26 ± 1.6	−19.1 ± 1.4	...	...	...	...
055	1.59 ± 1.2	−14.5 ± 0.7	0.43 ± 1.7	−2.2 ± 0.6	−0.60 ± 1.4	3.0 ± 0.6	...	...	...	...
056	1.00 ± 1.4	−6.3 ± 0.8	...	...	0.16 ± 1.0	−0.5 ± 0.4	1.29 ± 3.4	−4.7 ± 1.2	...	...
057	1.81 ± 1.0	−8.0 ± 0.5	...	−0.1 ± 0.2	1.25 ± 0.9	−2.3 ± 0.2	...	...	...	...
058	3.24 ± 1.1	−63.5 ± 1.0	1.18 ± 0.7	−38.4 ± 1.3	3.49 ± 1.1	−113.8 ± 1.5	...	...	...	...
059	2.65 ± 1.2	−30.6 ± 1.1	0.33 ± 1.0	−2.9 ± 0.9	0.77 ± 0.9	−7.1 ± 0.9	...	...	...	...
060	3.44 ± 1.1	−32.9 ± 1.4	0.57 ± 0.8	−5.0 ± 1.1	1.56 ± 0.8	−13.8 ± 1.3	...	...	...	...
061	2.81 ± 1.1	−33.6 ± 1.0	0.25 ± 0.8	−2.0 ± 0.6	0.73 ± 0.8	−6.0 ± 0.6	...	...	...	...
062	1.73 ± 1.2	−28.1 ± 0.9	...	0.1 ± 0.9	0.36 ± 0.8	−4.1 ± 0.5	1.16 ± 2.7	−17.3 ± 2.0	0.60 ± 3.5	−10.1 ± 2.9
063	2.98 ± 1.0	−35.3 ± 1.1	...	...	1.54 ± 0.8	−16.6 ± 0.9	...	...	...	...
064	2.65 ± 1.7	−37.4 ± 0.9	1.36 ± 1.1	−9.3 ± 0.3	4.49 ± 1.4	−30.2 ± 0.3	4.24 ± 1.5	−24.1 ± 0.3	3.91 ± 3.0	−22.2 ± 0.6
065	1.41 ± 2.6	−65.8 ± 1.7	1.87 ± 1.2	−104.1 ± 0.9	6.02 ± 1.7	−339.0 ± 1.1	...	−1.2 ± 1.1	0.19 ± 1.1	−14.4 ± 1.1
066	2.63 ± 0.9	−39.1 ± 2.2	0.82 ± 0.6	−18.5 ± 2.5	2.08 ± 0.7	−48.4 ± 2.6	...	...	...	...
067	3.59 ± 1.3	−44.3 ± 2.8	0.22 ± 0.8	−2.3 ± 1.7	1.29 ± 1.0	−12.8 ± 2.7	...	...	...	...
068	6.09 ± 0.8	−29.0 ± 2.8	1.30 ± 0.6	−5.2 ± 2.8	2.18 ± 0.6	−8.5 ± 2.2	...	...	...	...
069	3.59 ± 1.8	−53.5 ± 2.6	0.42 ± 0.9	−4.6 ± 1.1	1.97 ± 1.0	−21.9 ± 1.1	0.36 ± 1.1	−6.5 ± 2.5	1.07 ± 1.4	−21.4 ± 2.6
070	1.51 ± 0.5	−38.0 ± 1.0	0.07 ± 0.6	−1.6 ± 1.1	0.53 ± 0.5	−11.4 ± 0.9	...	...	...	...
071	4.16 ± 1.3	−58.5 ± 1.0	1.04 ± 1.2	−14.6 ± 1.0	0.97 ± 0.8	−13.7 ± 0.8	...	...	...	...
072	2.44 ± 1.3	−34.6 ± 2.0	0.20 ± 0.7	−2.4 ± 1.2	0.77 ± 0.8	−9.6 ± 1.2	...	...	...	...
073	1.90 ± 1.3	−24.3 ± 0.6	0.13 ± 1.0	−1.2 ± 0.4	0.33 ± 1.3	−3.2 ± 0.7	1.47 ± 2.7	−24.0 ± 1.5	1.90 ± 3.8	−36.9 ± 2.7
074	...	...	1.22 ± 1.1	−56.8 ± 0.3	3.72 ± 1.6	−175.3 ± 0.5	0.18 ± 0.9	−13.3 ± 0.8	0.73 ± 1.9	−55.3 ± 1.1
075	...	...	0.89 ± 1.1	−6.6 ± 0.5	2.07 ± 1.3	−15.4 ± 0.5	−0.20 ± 1.6	2.4 ± 1.2	0.79 ± 2.6	−9.1 ± 1.6
076	2.04 ± 1.1	−12.1 ± 0.3	0.18 ± 1.0	−0.7 ± 0.3	0.39 ± 0.9	−1.6 ± 0.2	1.02 ± 2.0	−7.0 ± 0.8	0.98 ± 3.6	−8.3 ± 1.7
077	1.57 ± 1.2	−9.0 ± 0.3	0.10 ± 1.0	−0.4 ± 0.2	0.31 ± 1.0	−1.3 ± 0.2	1.33 ± 1.9	−9.0 ± 0.6	1.10 ± 2.8	−8.6 ± 1.2
078	1.85 ± 1.0	−16.5 ± 1.0	...	−0.7 ± 1.3	0.82 ± 1.8	−4.7 ± 1.3	...	...	...	...
079	2.32 ± 1.0	−20.3 ± 1.5	0.13 ± 0.9	−0.7 ± 1.1	0.58 ± 0.9	−3.0 ± 1.1	...	...	...	...
080	2.24 ± 1.0	−37.3 ± 1.1	0.30 ± 0.8	−3.8 ± 0.8	1.14 ± 0.8	−14.4 ± 0.8	0.51 ± 2.2	−11.6 ± 4.1	0.42 ± 3.3	−12.6 ± 8.1

Table 8. continued.

	[OII]λ3727		[OIII]λ4959		[OIII]λ5007		[NII]λ6584		[SII]λλ6717+6731	
LCL05	flux	EW	flux	EW	flux	EW	flux	EW	flux	EW
081	2.19 ± 1.1	−29.6 ± 2.7	0.41 ± 0.9	−5.1 ± 3.2	1.38 ± 1.1	−18.0 ± 3.1	...	...	...	...
082	−2.03 ± 0.7	−8.9 ± 0.6	−0.39 ± 0.7	−0.8 ± 0.3	−0.57 ± 0.7	−1.2 ± 0.3	...	...	...	...
083	3.60 ± 0.7	−76.8 ± 0.9	1.07 ± 0.6	−24.9 ± 1.1	3.08 ± 1.2	−71.6 ± 2.0	...	...	...	...
084	5.13 ± 1.4	−46.0 ± 1.4	1.00 ± 1.1	−6.5 ± 1.0	2.34 ± 1.2	−14.8 ± 1.0	1.81 ± 1.5	−15.9 ± 3.8	...	...
085	5.47 ± 0.4	−50.0 ± 1.8	0.98 ± 0.4	−8.3 ± 2.7	3.47 ± 0.5	−29.3 ± 3.0	...	...	...	...
086	2.67 ± 0.8	−46.2 ± 2.3	0.51 ± 0.6	−5.7 ± 1.4	1.90 ± 0.7	−20.7 ± 1.4	...	...	...	...
087	2.36 ± 0.9	−50.4 ± 2.0	0.70 ± 0.7	−19.3 ± 2.5	1.62 ± 0.8	−36.2 ± 2.0	...	...	...	...
088	2.50 ± 0.8	−54.6 ± 1.7	1.64 ± 0.9	−41.9 ± 2.3	5.26 ± 1.3	−128.8 ± 4.0	...	...	...	...
089	6.68 ± 1.4	−22.3 ± 1.1	1.52 ± 1.9	−3.9 ± 1.3	2.29 ± 1.8	−5.9 ± 1.3	...	...	...	...
090	6.04 ± 1.4	−41.0 ± 1.3	1.19 ± 1.9	−6.3 ± 1.6	4.83 ± 1.7	−27.1 ± 1.8	...	...	...	...
091	1.95 ± 0.7	−21.3 ± 0.8	0.69 ± 1.0	−6.2 ± 1.7	1.19 ± 1.3	−11.4 ± 1.7	...	...	...	...
092	2.92 ± 1.1	−67.8 ± 1.0	1.15 ± 0.9	−33.3 ± 1.0	3.35 ± 1.1	−98.1 ± 1.1	...	...	...	...
093	2.91 ± 0.6	−58.6 ± 1.4	0.69 ± 0.6	−14.5 ± 1.6	1.70 ± 0.6	−36.5 ± 1.6	...	...	...	...
094	−12.57 ± 1.1	−44.6 ± 2.5	−1.32 ± 1.3	−4.9 ± 4.1	−11.26 ± 1.9	−40.6 ± 4.5	...	...	...	...
095	1.12 ± 0.7	−28.8 ± 1.6	0.18 ± 0.5	−3.4 ± 1.0	0.63 ± 0.5	−11.6 ± 0.9	...	...	...	...
096	4.95 ± 1.4	−32.9 ± 1.5	...	−0.3 ± 1.1	1.54 ± 0.9	−8.7 ± 1.1	...	...	...	...
097	19.85 ± 1.6	−19.3 ± 1.5	−0.54 ± 2.0	0.5 ± 2.1	18.34 ± 2.1	−17.2 ± 2.3	...	...	...	...
098	4.20 ± 1.3	−31.0 ± 2.9	1.96 ± 1.8	−15.0 ± 4.7	1.79 ± 1.8	−12.8 ± 4.9	...	...	...	...
099	2.29 ± 1.0	−21.5 ± 1.0	0.24 ± 0.8	−1.6 ± 0.6	0.66 ± 0.8	−4.5 ± 0.6	...	...	...	...
100	2.80 ± 1.0	−38.3 ± 1.1	0.50 ± 0.7	−5.8 ± 0.8	1.51 ± 0.8	−17.3 ± 0.8	...	...	...	...
101	4.70 ± 1.3	−21.5 ± 1.4	0.24 ± 1.0	−0.7 ± 0.9	1.25 ± 1.0	−3.6 ± 0.9	...	...	...	...
102	3.03 ± 0.8	−16.5 ± 0.8	0.08 ± 0.7	−0.2 ± 0.3	0.32 ± 0.7	−0.8 ± 0.3	...	...	...	...
103	3.65 ± 1.2	−28.7 ± 0.8	0.42 ± 1.6	−2.6 ± 1.0	1.15 ± 1.1	−7.1 ± 0.8	...	...	...	...
104	1.64 ± 1.0	−18.8 ± 1.4	...	−0.1 ± 0.8	0.41 ± 1.4	−2.5 ± 1.3	...	...	...	...
105	3.37 ± 0.4	−11.0 ± 0.5	0.68 ± 0.8	−0.8 ± 0.4	1.92 ± 0.8	−2.1 ± 0.4	...	...	...	...
106	2.91 ± 0.4	−83.1 ± 2.9	0.57 ± 0.8	−12.2 ± 4.7	2.92 ± 0.7	−60.8 ± 4.4	...	...	...	...
107	4.15 ± 0.7	−68.3 ± 2.8	0.66 ± 1.1	−5.3 ± 2.9	1.98 ± 2.0	−13.8 ± 5.2	...	...	...	...
108	1.94 ± 0.5	−8.3 ± 1.2	−1.13 ± 1.1	1.2 ± 0.8	1.22 ± 1.3	−1.3 ± 1.0	...	...	...	...
109	1.38 ± 0.3	−117.2 ± 0.9	2.47 ± 1.2	−309.3 ± 8.4	6.17 ± 1.4	−624.0 ± 6.2	...	...	...	...
110	0.76 ± 0.1	−3.9 ± 0.2	−0.14 ± 0.9	0.4 ± 1.1	2.13 ± 1.1	−7.3 ± 1.7	...	...	...	...
111	5.59 ± 1.5	−15.9 ± 0.5	0.44 ± 1.0	−0.5 ± 0.3	0.93 ± 1.7	−1.1 ± 0.3	...	...	...	...
112	1.06 ± 1.0	−6.6 ± 0.3	...	−0.2 ± 0.2	0.35 ± 0.9	−0.9 ± 0.1	...	...	...	...
113	1.91 ± 0.3	−28.8 ± 0.7	0.25 ± 1.1	−2.6 ± 2.6	2.01 ± 1.2	−18.0 ± 2.9	...	...	...	...
114	1.26 ± 0.5	−10.4 ± 0.5	...	−0.1 ± 0.5	1.06 ± 0.9	−3.7 ± 0.5	...	...	...	...
115	4.24 ± 1.5	−3.0 ± 0.8	4.71 ± 2.0	−1.0 ± 0.3	5.76 ± 1.7	−1.2 ± 0.3	...	...	...	...
116	0.99 ± 0.9	−2.0 ± 0.5	−0.17 ± 0.9	0.1 ± 0.2	1.02 ± 0.8	−0.7 ± 0.2	...	...	...	...
117	0.52 ± 0.9	−8.1 ± 0.5	...	−0.2 ± 0.3	...	−0.1 ± 0.3	...	...	...	...
118	0.73 ± 1.2	−8.9 ± 0.5	...	...	0.22 ± 1.3	−1.7 ± 0.4	...	...	...	...
119	1.29 ± 0.7	−17.7 ± 0.5	0.24 ± 1.9	−1.7 ± 0.8	0.46 ± 1.5	−3.4 ± 0.8	...	...	...	...
120	3.13 ± 1.1	−44.0 ± 2.1	1.08 ± 1.0	−13.3 ± 2.1	2.62 ± 1.4	−30.3 ± 3.2	...	...	...	...
121	1.58 ± 0.8	−43.7 ± 2.5	0.23 ± 1.8	−2.3 ± 2.5	0.78 ± 1.8	−6.9 ± 2.6	...	...	...	...
122	2.27 ± 0.3	−41.6 ± 0.6	0.61 ± 0.5	−10.3 ± 1.7	2.39 ± 0.6	−40.5 ± 1.4	...	...	...	...
123	2.13 ± 0.7	−57.4 ± 1.4	0.80 ± 0.8	−15.6 ± 1.7	1.66 ± 1.8	−32.6 ± 2.9	...	...	...	...
124	2.02 ± 0.6	−46.4 ± 0.5	0.37 ± 1.3	−7.2 ± 1.3	0.85 ± 1.6	−16.7 ± 1.4	...	...	...	...
125	2.74 ± 1.1	−25.3 ± 3.1	...	...	0.92 ± 1.2	−4.6 ± 2.9	...	...	...	...
126	0.59 ± 0.9	−5.9 ± 0.4	0.15 ± 1.2	−1.0 ± 0.4	0.38 ± 2.6	−2.5 ± 0.7	...	...	...	...
127	3.29 ± 0.7	−32.0 ± 1.3	0.73 ± 1.6	−5.6 ± 3.4	1.10 ± 2.0	−8.4 ± 3.2	...	...	...	...
128	3.00 ± 2.0	−37.1 ± 0.9	0.46 ± 1.3	−4.6 ± 0.7	1.25 ± 1.4	−12.4 ± 0.6	...	...	...	...
129	2.66 ± 0.6	−47.5 ± 2.4	1.04 ± 1.4	−12.2 ± 6.2	2.48 ± 1.8	−30.6 ± 6.2	...	...	...	...
130	13.85 ± 2.0	−18.3 ± 3.5	...	...	11.27 ± 1.6	−9.0 ± 1.7	...	...	...	...
131	2.29 ± 0.6	−92.3 ± 1.5	0.63 ± 2.6	−32.8 ± 9.2	3.06 ± 1.7	−140.8 ± 7.4	...	...	...	...
132	3.77 ± 0.6	−47.7 ± 2.1	1.13 ± 0.6	−11.7 ± 2.1	3.30 ± 0.6	−33.5 ± 1.8	...	...	...	...
133	2.14 ± 1.8	−43.7 ± 3.3	0.86 ± 1.1	−19.4 ± 2.7	2.65 ± 1.4	−59.7 ± 2.5	...	−1.2 ± 5.8	...	−1.1 ± 9.1
134	2.08 ± 0.8	−19.2 ± 0.9	0.24 ± 0.9	−1.5 ± 0.8	0.95 ± 0.8	−6.0 ± 0.6	...	...	...	...
135	0.99 ± 0.4	−21.5 ± 0.3	0.61 ± 1.4	−8.9 ± 0.9	1.16 ± 1.6	−17.7 ± 0.9	...	...	...	...
136	0.77 ± 1.2	−11.1 ± 1.6	...	...	0.13 ± 1.1	−0.8 ± 1.0	...	...	...	...
137	2.02 ± 1.0	−18.0 ± 0.5	...	−0.4 ± 0.8	...	0.3 ± 0.8	...	...	...	...
138	2.81 ± 0.7	−29.8 ± 1.7	0.47 ± 0.9	−3.1 ± 1.6	1.17 ± 1.0	−7.3 ± 2.9	...	...	...	...
139	2.70 ± 0.6	−73.9 ± 1.1	0.66 ± 0.9	−24.7 ± 3.2	2.95 ± 1.8	−159.6 ± 6.3	...	...	...	...
140	2.86 ± 0.5	−60.1 ± 2.6	0.74 ± 0.8	−10.1 ± 3.1	3.12 ± 1.5	−40.7 ± 4.6	...	...	...	...
141	10.24 ± 0.5	−34.8 ± 1.8	0.69 ± 0.2	−2.1 ± 1.1	2.19 ± 0.3	−7.4 ± 1.1	1.98 ± 0.7	−5.7 ± 2.7	1.35 ± 2.7	−6.7 ± 14.7
142	0.82 ± 0.8	−19.9 ± 3.2	1.80 ± 1.1	−54.5 ± 4.9	5.82 ± 1.3	−184.7 ± 5.2	...	...	...	...
143	1.40 ± 0.8	−9.3 ± 1.9	1.76 ± 0.8	−10.8 ± 1.6	−0.32 ± 0.9	2.0 ± 3.1	...	...	...	...

Table 9. Measurements of Balmer emission lines. Fluxes are given in $f(H\beta)$ units, associated errors in $\sigma[f(H\beta)]$ units, $H\beta$ flux and associated error are given in 10^{-17} erg s^{-1} cm^{-2} unit. Equivalent widths are given in Å, the *abs* column gives the equivalent width in absorption.

			Hα			Hβ			Hγ			Hδ
LCL05	flux	EW	abs	flux	EW	abs	flux	EW	abs	flux	EW	abs
001	...	...	0.0	5.73 ± 0.8	−8.1 ± 1.3	3.7	0.25 ± 0.9	−2.0 ± 1.3	2.6	0.51 ± 0.9	−3.7 ± 1.2	4.3
002	...	...	0.0	11.79 ± 1.7	−10.9 ± 1.7	1.6	0.25 ± 0.4	−3.2 ± 0.9	2.8	0.12 ± 0.3	−1.4 ± 0.8	4.4
003	...	...	0.0	19.27 ± 0.8	−15.0 ± 0.7	4.6	0.42 ± 0.9	−5.6 ± 0.7	3.7	0.32 ± 0.8	−3.9 ± 0.6	4.4
004	4.08 ± 2.2	−29.8 ± 1.5	2.3	6.97 ± 0.5	−6.7 ± 0.6	3.7	0.59 ± 0.9	−3.5 ± 0.5	2.8	0.52 ± 1.0	−2.9 ± 0.5	4.8
005	1.18 ± 1.6	−1.2 ± 0.4	1.0	3.84 ± 0.5	−0.9 ± 0.2	1.7	0.91 ± 0.9	−1.1 ± 0.2	0.1	0.40 ± 0.9	−0.6 ± 0.3	0.6
006	3.05 ± 1.8	−39.9 ± 2.5	3.1	5.36 ± 0.6	−8.0 ± 1.1	1.7	0.42 ± 0.9	−3.0 ± 1.0	3.2	0.44 ± 0.9	−3.3 ± 1.0	2.5
007	9.11 ± 2.2	−14.0 ± 1.3	3.3	2.32 ± 0.6	−1.3 ± 0.5	2.3	0.19 ± 0.9	−0.3 ± 0.5	1.5	1.02 ± 1.0	−1.4 ± 0.5	3.4
008	3.02 ± 1.8	−36.2 ± 1.5	2.8	8.02 ± 0.5	−8.8 ± 0.8	1.9	0.32 ± 0.9	−2.5 ± 0.7	2.0	0.24 ± 0.8	−1.8 ± 0.7	3.5
009	2.90 ± 2.3	−22.4 ± 1.9	2.7	8.63 ± 0.8	−4.9 ± 0.6	3.6	0.67 ± 0.9	−3.2 ± 1.1	2.3	0.18 ± 0.8	−0.9 ± 0.6	4.6
010	7.14 ± 3.5	−26.8 ± 1.8	1.4	3.39 ± 0.5	−3.9 ± 0.8	2.5	0.27 ± 0.9	−1.2 ± 1.0	1.8	0.57 ± 0.9	−2.8 ± 1.0	2.6
011	5.94 ± 2.6	−36.1 ± 2.0	5.9	3.76 ± 0.5	−4.5 ± 1.0	4.0	0.70 ± 0.9	−2.7 ± 0.7	2.9	0.61 ± 0.9	−2.3 ± 0.7	3.9
012	2.77 ± 1.3	−7.7 ± 1.0	2.1	1.67 ± 0.4	−2.7 ± 1.0	3.1	...	−0.1 ± 1.3	2.9	1.33 ± 1.3	−4.1 ± 1.6	3.2
013	...	...	0.0	1.67 ± 0.5	−4.4 ± 1.4	3.5	0.49 ± 0.8	−2.2 ± 1.4	2.2	...	...	4.4
014	...	...	0.0	2.74 ± 0.5	−4.3 ± 0.8	4.1	0.25 ± 0.7	−1.2 ± 0.8	4.1	0.16 ± 0.7	−0.8 ± 0.9	4.9
015	3.27 ± 2.1	−51.9 ± 4.0	3.0	2.39 ± 0.3	−9.0 ± 1.4	3.7	0.31 ± 0.9	−2.3 ± 1.2	4.2	0.35 ± 0.9	−2.7 ± 1.2	5.8
016	3.55 ± 2.3	−181.4 ± 2.7	5.2	15.10 ± 0.3	−27.1 ± 1.0	4.0	0.51 ± 1.0	−11.6 ± 0.7	2.2	0.29 ± 0.9	−6.0 ± 0.6	3.6
017	5.61 ± 1.9	−1.8 ± 1.2	1.5	0.16 ± 0.3	−0.3 ± 0.7	2.9	−0.91 ± 0.9	0.4 ± 0.9	1.2	1.74 ± 0.9	−0.7 ± 0.9	2.8
018	...	...	0.0	4.65 ± 0.8	−7.2 ± 1.4	3.1	0.54 ± 0.6	−3.6 ± 1.0	3.7	0.63 ± 0.6	−4.2 ± 1.1	5.3
019	3.01 ± 2.0	−80.1 ± 4.2	5.6	5.77 ± 0.3	−17.1 ± 1.5	1.9	...	...	0.0	...	...	0.0
020	...	...	0.0	3.28 ± 1.2	−7.6 ± 3.8	3.3	0.51 ± 0.7	−3.6 ± 2.7	3.4	0.16 ± 0.7	−1.1 ± 2.5	4.0
021	3.38 ± 2.5	−70.8 ± 2.9	6.8	13.15 ± 0.6	−13.1 ± 0.8	3.5	0.46 ± 0.9	−5.6 ± 0.8	4.1	0.14 ± 0.9	−1.5 ± 0.7	5.8
022	...	...	0.0	8.84 ± 0.9	−18.7 ± 2.5	1.2	0.41 ± 0.5	−6.4 ± 1.0	3.7	0.19 ± 0.4	−2.6 ± 0.9	3.7
023	...	...	0.0	10.71 ± 0.6	−12.1 ± 0.8	4.3	0.28 ± 0.8	−3.0 ± 0.7	3.6	0.25 ± 0.8	−2.4 ± 0.7	3.6
024	...	...	0.0	10.46 ± 0.7	−23.1 ± 2.3	5.4	0.42 ± 0.6	−8.4 ± 1.6	2.1	0.22 ± 0.6	−4.3 ± 1.3	4.0
025	...	...	0.0	3.18 ± 0.6	−5.5 ± 1.2	2.3	0.27 ± 0.8	−1.3 ± 1.1	3.1	...	0.3 ± 1.0	6.1
026	...	...	0.0	7.31 ± 0.6	−14.9 ± 1.5	2.8	0.40 ± 0.8	−5.1 ± 1.3	3.4	0.26 ± 0.8	−3.1 ± 1.2	4.3
027	...	...	0.0	4.07 ± 0.5	−19.9 ± 2.9	3.9	0.52 ± 0.9	−9.3 ± 2.6	1.6	0.29 ± 0.8	−5.0 ± 2.5	5.0
028	3.92 ± 2.2	−36.6 ± 0.8	1.4	16.34 ± 0.6	−6.3 ± 0.3	2.8	0.42 ± 0.9	−2.8 ± 0.3	2.5	0.26 ± 0.9	−1.6 ± 0.3	3.7
029	...	...	0.0	2.32 ± 0.7	−4.0 ± 1.8	2.2	0.81 ± 0.8	−3.3 ± 1.3	2.3	0.18 ± 0.8	−0.7 ± 1.4	3.6
030	...	...	0.0	3.72 ± 1.4	−15.7 ± 6.9	2.2	0.29 ± 0.4	−3.1 ± 2.2	2.8	0.10 ± 0.3	−1.1 ± 2.1	3.9
031	3.79 ± 2.1	−66.0 ± 3.9	3.3	4.63 ± 0.4	−13.0 ± 1.6	2.8	0.50 ± 0.9	−5.8 ± 1.4	2.5	0.19 ± 0.9	−2.1 ± 1.4	4.5
032	...	...	0.0	5.07 ± 0.5	−7.3 ± 1.0	4.0	0.38 ± 1.0	−2.7 ± 1.4	3.0	0.28 ± 0.8	−1.8 ± 1.0	4.2
033	8.32 ± 1.8	−23.0 ± 1.1	1.2	2.21 ± 0.5	−2.3 ± 0.7	2.2	0.40 ± 1.9	−1.0 ± 1.6	0.6	...	...	2.5
034	3.20 ± 3.4	−48.8 ± 3.9	3.2	8.10 ± 0.5	−8.8 ± 0.7	3.6	0.43 ± 0.9	−3.2 ± 0.7	5.5	0.23 ± 0.8	−1.5 ± 0.6	5.1
035	...	...	0.0	9.05 ± 0.6	−10.8 ± 1.2	3.7	0.48 ± 0.8	−4.5 ± 1.0	3.6	0.29 ± 0.7	−2.4 ± 0.7	4.6
036	3.87 ± 1.9	−59.3 ± 1.1	1.3	23.79 ± 0.8	−12.1 ± 0.6	0.9	0.44 ± 0.7	−4.8 ± 0.3	1.6	0.24 ± 0.6	−2.4 ± 0.3	2.4
037	...	...	0.0	6.15 ± 0.6	−3.7 ± 0.5	3.1	0.69 ± 0.8	−2.8 ± 0.5	2.2	0.73 ± 0.9	−2.9 ± 0.5	4.0
038	2.90 ± 1.8	−41.8 ± 1.0	3.8	25.42 ± 0.8	−9.6 ± 0.4	2.7	0.45 ± 0.8	−3.8 ± 0.3	2.7	0.27 ± 0.8	−2.1 ± 0.3	3.5
039	3.34 ± 2.0	−38.2 ± 1.8	3.8	10.41 ± 0.6	−6.7 ± 0.8	3.6	0.60 ± 0.9	−3.9 ± 0.5	3.6	0.47 ± 0.8	−2.8 ± 0.5	5.3
040	...	...	0.0	13.37 ± 0.9	−22.8 ± 1.9	3.4	0.34 ± 0.6	−6.9 ± 1.1	3.5	0.14 ± 0.5	−2.4 ± 0.9	3.8
041	...	...	0.0	2.22 ± 0.4	−14.7 ± 3.2	4.4	−0.20 ± 0.7	3.1 ± 2.9	4.8	...	0.3 ± 2.6	2.9
042	...	...	0.0	4.38 ± 0.3	−27.1 ± 2.6	2.4	0.28 ± 1.0	−6.9 ± 3.1	3.3	0.16 ± 1.2	−3.0 ± 3.5	2.7
043	...	...	0.0	1.95 ± 0.4	−8.0 ± 1.9	4.0	0.53 ± 0.8	−4.1 ± 1.7	3.1	0.22 ± 0.8	−1.6 ± 1.6	4.6
044	...	...	0.0	6.36 ± 0.7	−4.3 ± 0.6	3.7	0.27 ± 1.8	−1.1 ± 0.8	2.4	0.72 ± 0.8	−3.1 ± 0.5	4.2
045	...	...	0.0	28.77 ± 0.5	−58.2 ± 1.2	3.4	0.41 ± 1.0	−21.3 ± 1.2	3.2	0.21 ± 0.9	−9.7 ± 1.1	1.4
046	...	...	0.0	8.28 ± 0.7	−15.8 ± 1.6	2.9	0.21 ± 0.5	−3.4 ± 1.0	2.9	0.11 ± 0.4	−1.7 ± 1.0	4.6
047	...	...	0.0	1.98 ± 0.3	−16.9 ± 3.5	1.1	0.40 ± 0.8	−5.9 ± 2.9	2.2	0.09 ± 0.8	−1.4 ± 3.0	4.6
048	...	...	0.0	0.04 ± 0.4	...	3.0	13.82 ± 0.9	−2.3 ± 2.2	3.4	9.25 ± 0.9	−1.7 ± 2.3	5.6
049	5.27 ± 2.0	−33.6 ± 0.8	2.4	7.37 ± 0.4	−5.6 ± 0.5	3.2	0.42 ± 0.9	−2.5 ± 0.5	3.0	0.28 ± 0.8	−1.7 ± 0.5	3.7
050	...	...	0.0	9.43 ± 0.6	−30.1 ± 2.7	2.1	0.32 ± 0.6	−9.3 ± 1.6	2.2	0.15 ± 0.7	−4.1 ± 2.1	4.0
051	...	...	0.0	16.97 ± 0.4	−41.2 ± 1.3	3.7	0.44 ± 0.9	−15.1 ± 1.1	2.8	0.25 ± 1.0	−7.7 ± 1.1	2.2
052	3.20 ± 3.3	−206.8 ± 5.0	7.2	22.31 ± 0.5	−34.0 ± 1.0	0.6	0.43 ± 0.8	−13.8 ± 1.2	−0.3	0.23 ± 0.7	−6.9 ± 0.8	2.3
053	...	...	0.0	19.46 ± 1.2	−16.3 ± 1.0	4.4	0.39 ± 0.5	−5.2 ± 0.6	4.9	0.34 ± 0.8	−4.4 ± 1.3	1.9
054	...	...	0.0	14.57 ± 0.7	−13.8 ± 0.9	4.8	0.47 ± 0.7	−4.9 ± 0.4	4.9	0.24 ± 0.8	−2.4 ± 0.8	4.7
055	...	...	0.0	14.26 ± 0.9	−5.0 ± 0.3	3.3	0.13 ± 0.8	−0.8 ± 0.6	4.3	0.17 ± 0.8	−0.9 ± 0.4	3.9
056	4.69 ± 3.6	−16.7 ± 1.0	1.6	8.01 ± 0.7	−3.3 ± 0.4	3.3	0.45 ± 0.9	−1.7 ± 0.5	2.3	0.27 ± 0.8	−1.1 ± 0.4	3.8
057	...	...	0.0	8.16 ± 0.8	−1.8 ± 0.3	2.7	0.74 ± 1.0	−1.7 ± 0.3	1.5	0.74 ± 0.9	−1.8 ± 0.3	2.8
058	...	...	0.0	16.70 ± 0.7	−33.9 ± 3.3	4.1	0.51 ± 0.8	−9.1 ± 0.9	3.7	0.31 ± 0.7	−4.9 ± 0.7	4.7
059	...	...	0.0	10.12 ± 0.8	−9.1 ± 0.8	4.5	0.51 ± 0.9	−4.4 ± 0.8	5.3	0.47 ± 0.8	−3.9 ± 0.7	5.9
060	...	...	0.0	5.40 ± 0.6	−8.9 ± 1.2	4.3	0.66 ± 1.6	−4.7 ± 1.6	4.6	0.66 ± 1.7	−4.5 ± 2.2	3.3
061	...	...	0.0	9.58 ± 0.6	−8.0 ± 0.6	4.3	0.20 ± 1.5	−1.5 ± 0.9	4.4	−0.59 ± 1.4	4.3 ± 1.2	3.8
062	3.92 ± 3.3	−58.6 ± 2.0	1.4	13.73 ± 0.6	−11.3 ± 0.6	2.3	0.26 ± 2.3	−2.8 ± 1.1	2.8	0.13 ± 0.7	−1.4 ± 0.5	4.2
063	...	...	0.0	7.79 ± 0.6	−10.4 ± 1.0	6.2	0.26 ± 2.2	−2.5 ± 1.9	2.4	0.09 ± 0.5	−0.8 ± 0.6	3.3
064	6.59 ± 1.9	−37.0 ± 0.3	1.7	7.35 ± 0.3	−6.8 ± 0.3	2.0	0.38 ± 0.9	−3.3 ± 0.4	1.3	0.31 ± 1.0	−3.0 ± 0.4	1.8
065	3.70 ± 1.4	−284.6 ± 1.1	4.2	21.06 ± 0.3	−52.0 ± 0.7	−3.8	0.47 ± 1.1	−22.1 ± 0.9	−2.8	0.20 ± 1.2	−8.3 ± 0.8	0.9
066	...	...	0.0	1.89 ± 0.3	−24.9 ± 4.3	6.5	1.27 ± 0.9	−23.0 ± 3.1	2.6	...	1.1 ± 3.1	1.2
067	...	...	0.0	2.25 ± 0.4	−10.4 ± 2.0	3.4	−0.32 ± 1.9	2.6 ± 3.4	2.4	0.47 ± 1.0	−3.9 ± 2.0	6.1
068	...	...	0.0	0.56 ± 0.4	−4.2 ± 4.0	2.9	1.07 ± 0.5	−3.9 ± 1.7	5.7	−0.12 ± 0.4	0.4 ± 1.7	4.4
069	3.34 ± 1.7	−60.0 ± 2.7	4.5	3.19 ± 0.3	−11.6 ± 1.2	0.1	0.29 ± 0.9	−3.4 ± 1.3	3.8	0.22 ± 0.9	−2.9 ± 1.5	2.1
070	...	...	0.0	8.52 ± 0.6	−22.9 ± 1.9	5.2	0.31 ± 0.4	−5.7 ± 0.9	4.2	0.21 ± 0.4	−4.1 ± 0.7	4.6
071	...	...	0.0	5.19 ± 0.3	−13.5 ± 0.9	4.2	0.44 ± 0.8	−5.4 ± 0.7	2.4	0.32 ± 1.0	−3.4 ± 0.7	3.6
072	...	...	0.0	3.29 ± 0.4	−11.2 ± 1.4	3.1	0.46 ± 0.9	−5.1 ± 1.4	3.3	0.17 ± 0.9	−1.8 ± 1.4	3.8
073	3.85 ± 2.6	−62.9 ± 1.4	5.4	7.95 ± 0.2	−9.2 ± 0.4	4.4	0.50 ± 0.8	−4.6 ± 0.3	4.5	0.34 ± 0.8	−2.9 ± 0.3	5.2
074	3.17 ± 1.7	−234.3 ± 0.7	1.3	56.84 ± 0.4	−45.5 ± 0.3	−2.8	0.42 ± 0.8	−15.8 ± 0.3	0.1	0.25 ± 0.8	−8.1 ± 0.3	1.5
075	2.95 ± 1.5	−34.4 ± 0.9	4.3	4.91 ± 0.2	−7.4 ± 0.5	3.8	0.43 ± 0.9	−2.9 ± 0.4	3.9	0.26 ± 1.0	−1.5 ± 0.4	5.7
076	5.26 ± 3.4	−35.2 ± 1.0	1.9	6.35 ± 0.3	−3.9 ± 0.2	4.3	0.31 ± 0.9	−1.2 ± 0.2	4.1	0.27 ± 0.8	−0.9 ± 0.2	5.8
077	3.41 ± 2.1	−22.5 ± 0.5	2.9	7.23 ± 0.3	−4.2 ± 0.3	3.5	0.39 ± 0.8	−1.5 ± 0.2	4.0	0.31 ± 0.8	−1.1 ± 0.2	4.9
078	...	...	0.0	3.50 ± 0.3	−5.4 ± 0.6	4.4	0.26 ± 0.6	−1.5 ± 0.5	3.7	0.24 ± 0.6	−1.3 ± 0.5	5.3
079	...	...	0.0	1.58 ± 0.3	−5.4 ± 1.1	3.8	0.54 ± 0.8	−3.1 ± 1.0	4.0	0.21 ± 0.7	−1.2 ± 1.0	4.8

Table 9. continued.

			Hα			Hβ			Hγ			Hδ
LCL05	flux	EW	abs	flux	EW	abs	flux	EW	abs	flux	EW	abs
080	1.85 ± 1.8	−41.7 ± 3.2	−0.1	6.46 ± 0.4	−12.9 ± 0.9	3.3	0.39 ± 0.8	−4.7 ± 0.8	4.1	0.23 ± 0.7	−2.7 ± 0.7	4.4
081	...	...	0.0	1.35 ± 0.2	−12.6 ± 2.5	2.2	0.46 ± 1.0	−5.5 ± 2.7	5.7	−0.27 ± 0.8	3.1 ± 2.3	5.0
082	...	...	0.0	−2.66 ± 0.5	2.1 ± 0.5	1.8	−0.12 ± 0.7	−0.3 ± 0.5	1.5	−0.32 ± 0.7	−0.8 ± 0.5	3.0
083	...	...	0.0	4.80 ± 0.3	−23.4 ± 1.7	8.5	0.44 ± 0.5	−8.5 ± 0.8	3.6	0.28 ± 0.4	−4.9 ± 0.6	4.2
084	4.27 ± 1.9	−37.8 ± 1.7	1.2	1.42 ± 0.2	−6.0 ± 0.9	1.4	0.46 ± 1.0	−2.7 ± 0.9	3.6	0.34 ± 1.0	−2.0 ± 0.9	4.4
085	...	...	0.0	0.84 ± 0.4	−8.6 ± 5.7	−1.6	0.09 ± 0.5	−0.6 ± 2.3	3.1	0.63 ± 0.5	−4.0 ± 1.9	3.9
086	...	...	0.0	1.70 ± 0.3	−10.2 ± 1.8	5.2	0.52 ± 0.7	−5.3 ± 1.6	4.1	0.44 ± 0.7	−4.1 ± 1.5	4.5
087	...	...	0.0	2.18 ± 0.2	−21.5 ± 2.7	7.0	0.68 ± 0.9	−13.7 ± 2.3	−0.1	−0.11 ± 0.8	1.8 ± 1.9	3.0
088	...	...	0.0	2.40 ± 0.2	−28.1 ± 2.7	3.5	0.41 ± 0.7	−7.2 ± 1.3	3.4	0.28 ± 0.5	−4.8 ± 1.2	4.7
089	...	...	0.0	0.89 ± 0.2	−2.6 ± 0.7	3.2	0.69 ± 0.8	−1.9 ± 0.7	2.6	0.73 ± 0.8	−2.0 ± 0.7	2.2
090	...	...	0.0	1.16 ± 0.1	−5.2 ± 0.9	3.1	0.97 ± 1.0	−5.2 ± 0.8	5.2	0.11 ± 0.9	−0.6 ± 0.8	4.6
091	...	...	0.0	3.40 ± 0.4	−8.9 ± 1.2	3.9	0.25 ± 1.0	−2.1 ± 1.1	4.0	0.30 ± 0.7	−2.4 ± 0.9	3.9
092	...	...	0.0	5.93 ± 0.2	−26.6 ± 1.0	2.3	0.39 ± 0.8	−8.8 ± 0.8	5.3	0.32 ± 0.7	−6.0 ± 0.7	5.2
093	...	...	0.0	4.25 ± 0.4	−19.8 ± 2.3	3.4	0.23 ± 0.4	−4.1 ± 1.1	4.7	0.17 ± 0.4	−2.7 ± 1.0	4.4
094	...	...	0.0	−0.40 ± 0.2	3.8 ± 3.0	1.8	−0.11 ± 0.9	−0.3 ± 2.4	2.4	−0.43 ± 0.9	−1.2 ± 2.1	3.4
095	...	...	0.0	3.15 ± 0.3	−20.6 ± 1.9	3.6	0.28 ± 0.8	−5.0 ± 1.6	4.2	...	−0.3 ± 1.4	4.6
096	...	...	0.0	1.26 ± 0.2	−5.4 ± 1.1	2.9	0.81 ± 1.1	−4.0 ± 1.2	6.0	1.09 ± 1.3	−5.1 ± 1.3	3.5
097	...	...	0.0	0.15 ± 0.1	−0.8 ± 1.1	1.6	3.22 ± 1.4	−2.6 ± 1.3	1.9	3.65 ± 1.1	−2.8 ± 1.1	2.8
098	...	...	0.0	0.55 ± 0.2	−6.7 ± 2.5	3.0	0.27 ± 0.9	−1.8 ± 2.6	6.5	0.17 ± 0.8	−1.0 ± 2.1	5.9
099	...	...	0.0	4.52 ± 0.4	−6.8 ± 0.8	4.1	0.32 ± 1.0	−2.3 ± 0.9	3.0	0.27 ± 0.8	−1.7 ± 1.2	3.2
100	...	...	0.0	4.62 ± 0.4	−11.6 ± 1.1	2.1	0.49 ± 0.9	−5.5 ± 1.2	2.5	...	−0.6 ± 1.3	4.7
101	...	...	0.0	1.16 ± 0.3	−2.8 ± 0.8	5.0	0.84 ± 1.0	−2.6 ± 1.1	1.2	0.47 ± 0.8	−1.2 ± 0.8	4.5
102	...	...	0.0	2.82 ± 0.4	−2.3 ± 0.4	2.9	0.33 ± 0.7	−0.9 ± 0.4	2.2	0.29 ± 0.7	−0.9 ± 0.5	2.8
103	...	...	0.0	4.81 ± 0.4	−6.0 ± 0.6	3.9	0.83 ± 0.9	−4.5 ± 0.6	4.6	0.46 ± 0.9	−2.5 ± 0.6	4.1
104	...	...	0.0	2.86 ± 0.3	−6.0 ± 0.8	3.9	0.44 ± 1.7	−3.0 ± 1.4	3.3	0.41 ± 0.9	−2.8 ± 1.0	3.2
105	...	...	0.0	1.10 ± 0.4	−1.1 ± 0.5	2.9	0.83 ± 0.4	−1.4 ± 0.3	1.9	1.08 ± 0.3	−1.9 ± 0.3	3.0
106	...	...	0.0	1.98 ± 0.5	−20.3 ± 5.6	5.7	0.31 ± 0.6	−7.1 ± 4.0	1.7	0.13 ± 0.3	−3.5 ± 3.1	4.0
107	...	...	0.0	0.96 ± 0.2	−8.9 ± 3.0	3.8	0.37 ± 0.5	−4.3 ± 2.0	3.7	0.27 ± 0.4	−3.2 ± 1.9	3.3
108	...	...	0.0	0.39 ± 0.2	−1.1 ± 0.8	2.4	1.29 ± 0.8	−2.1 ± 0.8	5.0	...	...	4.6
109	...	...	0.0	14.25 ± 0.5	−113.8 ± 6.5	−14.2	0.42 ± 0.4	−45.6 ± 2.1	−0.1	0.26 ± 0.4	−27.4 ± 2.0	2.6
110	...	...	0.0	4.15 ± 1.2	−2.3 ± 0.7	7.8	0.04 ± 0.3	−0.1 ± 0.3	5.3	0.60 ± 0.2	−1.4 ± 0.1	6.7
111	...	...	0.0	0.85 ± 0.1	−1.2 ± 0.2	3.1	1.19 ± 1.1	−1.6 ± 0.3	2.5	1.19 ± 0.9	−1.7 ± 0.2	3.6
112	...	...	0.0	3.19 ± 0.2	−2.5 ± 0.2	3.7	0.48 ± 0.6	−1.5 ± 0.1	2.7	0.65 ± 0.7	−2.1 ± 0.2	3.7
113	...	...	0.0	3.29 ± 0.6	−11.4 ± 2.6	2.6	0.15 ± 0.3	−1.8 ± 0.8	4.0	0.04 ± 0.2	−0.4 ± 0.7	4.8
114	...	...	0.0	1.86 ± 0.3	−3.5 ± 0.5	1.8	0.29 ± 0.5	−1.4 ± 0.4	4.0	0.26 ± 0.3	−1.2 ± 0.2	4.1
115	...	...	0.0	0.26 ± 0.2	−0.2 ± 0.2	2.0	1.27 ± 0.6	−0.4 ± 0.2	0.8	1.96 ± 0.7	−0.7 ± 0.2	1.5
116	...	...	0.0	1.20 ± 0.3	−0.7 ± 0.2	2.7	1.28 ± 0.6	−1.2 ± 0.2	0.7	1.26 ± 0.5	−1.3 ± 0.2	2.3
117	...	...	0.0	4.45 ± 0.2	−6.4 ± 0.2	3.3	0.28 ± 0.7	−2.3 ± 0.3	2.2	0.19 ± 0.7	−1.7 ± 0.3	3.4
118	...	...	0.0	3.61 ± 0.1	−7.5 ± 0.3	4.2	0.24 ± 0.8	−1.8 ± 0.3	4.3	0.33 ± 0.8	−2.4 ± 0.3	4.2
119	...	...	0.0	3.38 ± 0.2	−6.9 ± 0.4	2.9	0.39 ± 0.7	−3.3 ± 0.5	3.8	0.23 ± 0.7	−1.9 ± 0.4	3.1
120	...	...	0.0	0.62 ± 0.1	−12.6 ± 1.8	3.2	0.69 ± 0.8	−7.1 ± 1.6	4.2	0.28 ± 0.8	−2.9 ± 1.4	3.2
121	...	...	0.0	1.29 ± 0.1	−13.8 ± 1.8	5.2	−0.17 ± 0.6	2.0 ± 1.0	3.6	0.41 ± 0.9	−4.5 ± 1.3	3.5
122	...	...	0.0	4.16 ± 0.5	−15.7 ± 2.2	3.6	0.36 ± 0.4	−5.2 ± 1.1	4.5	0.19 ± 0.3	−2.4 ± 0.6	4.1
123	...	...	0.0	3.77 ± 0.3	−21.4 ± 2.0	3.9	0.27 ± 0.5	−5.0 ± 1.1	3.6	0.14 ± 0.4	−2.4 ± 1.0	4.8
124	...	...	0.0	6.73 ± 0.2	−18.2 ± 0.8	4.0	0.47 ± 0.9	−8.3 ± 0.6	2.8	0.19 ± 0.7	−2.9 ± 0.5	3.3
125	...	...	0.0	0.54 ± 0.2	−5.3 ± 1.8	2.4	0.82 ± 1.0	−4.8 ± 2.3	3.6	−0.10 ± 0.8	0.6 ± 1.9	4.8
126	...	...	0.0	3.84 ± 0.2	−7.0 ± 0.4	2.3	0.36 ± 0.6	−2.6 ± 0.3	5.7	0.22 ± 0.5	−1.6 ± 0.2	4.5
127	...	...	0.0	0.96 ± 0.2	−8.1 ± 1.9	2.8	...	0.6 ± 1.9	2.9	0.18 ± 0.9	−1.3 ± 1.5	6.6
128	...	...	0.0	3.02 ± 0.1	−9.7 ± 0.4	3.6	0.26 ± 0.9	−2.4 ± 0.4	3.6	0.13 ± 0.9	−1.1 ± 0.4	4.2
129	...	...	0.0	1.32 ± 0.3	−12.2 ± 2.6	2.9	0.24 ± 0.8	−3.3 ± 2.5	1.1	0.28 ± 0.6	−3.6 ± 2.1	2.4
130	...	...	0.0	0.06 ± 0.1	−0.8 ± 1.1	5.1	0.34 ± 1.0	−0.4 ± 1.8	5.0	3.14 ± 1.2	−2.5 ± 1.4	5.9
131	...	...	0.0	3.43 ± 0.2	−59.9 ± 4.6	3.8	0.35 ± 0.5	−14.5 ± 1.7	2.0	0.11 ± 0.6	−3.8 ± 1.9	4.1
132	...	...	0.0	0.99 ± 0.2	−10.9 ± 2.9	1.9	0.27 ± 0.5	−2.8 ± 1.7	4.8	0.38 ± 0.4	−3.4 ± 1.3	5.2
133	4.78 ± 5.5	−53.7 ± 5.4	−2.3	1.33 ± 0.1	−17.6 ± 1.6	2.7	0.28 ± 1.0	−4.0 ± 1.7	7.0	0.32 ± 1.1	−3.3 ± 1.2	4.5
134	...	...	0.0	1.69 ± 0.2	−6.0 ± 0.8	3.5	0.36 ± 0.5	−2.2 ± 0.5	3.6	0.47 ± 0.5	−2.9 ± 0.5	3.8
135	...	...	0.0	11.67 ± 0.3	−15.3 ± 0.5	2.8	0.33 ± 0.4	−5.2 ± 0.3	1.3	0.20 ± 0.5	−3.5 ± 0.4	2.3
136	...	...	0.0	11.37 ± 0.6	−6.9 ± 0.7	2.9	0.58 ± 1.0	−3.9 ± 0.9	4.2	0.15 ± 0.8	−1.0 ± 0.7	3.1
137	...	...	0.0	11.46 ± 0.4	−9.1 ± 0.5	1.6	0.16 ± 0.5	−1.3 ± 0.3	0.6	0.05 ± 0.5	−0.4 ± 0.3	1.4
138	...	...	0.0	4.48 ± 0.6	−7.2 ± 1.8	3.1	0.94 ± 0.8	−7.0 ± 2.1	3.6	0.87 ± 0.7	−6.0 ± 1.4	4.0
139	...	...	0.0	15.98 ± 0.6	−20.8 ± 1.4	3.1	0.44 ± 0.5	−10.1 ± 1.0	3.9	0.18 ± 0.4	−3.9 ± 0.7	1.2
140	...	...	0.0	4.54 ± 0.6	−11.7 ± 3.8	0.6	0.50 ± 0.5	−6.4 ± 2.1	−0.9	0.27 ± 0.4	−3.6 ± 1.8	1.2
141	14.11 ± 1.0	−40.6 ± 2.8	0.9	1.76 ± 1.2	−3.1 ± 4.2	2.7	1.68 ± 0.4	−4.3 ± 1.4	2.5	0.79 ± 0.4	−2.0 ± 1.3	3.2
142	3.79 ± 3.3	−172.6 ± 20.9	6.5	3.77 ± 0.3	−31.2 ± 5.8	−7.5	0.30 ± 0.6	−10.5 ± 4.0	−6.6	0.16 ± 0.6	−4.7 ± 3.7	1.5
143	...	...	0.0	0.80 ± 0.2	−5.8 ± 2.1	2.0	...	...	2.8	1.85 ± 1.2	−9.1 ± 2.2	5.1